We thank the Referee for his/her time and his/her constructive comments. We have complied with most of the proposed changes. In the following, the comments made by the Referee appear in black, while our replies are in blue.

The paper contains a comprehensive case study analysis of convection embedded in a warm conveyor belt and its impact on the upper-level flow. The study combines unique observations taken during the North Atlantic Waveguide and Downstream Impact Experiment and convection-permitting simulations of the case study. The observations are compared to a reference simulation and an experiment in which heat exchanges due to cloud processes are turned off (called NODIA). Generally, the reference simulation agrees with the observations whereas key features are missing in the NODIA experiment, highlighting their diabatic origin. In particular, elongated bands of absolute negative PV are missing in the NODIA simulation. Their impact on the upper-level flow is hence missing in NODIA. These findings support the theory developed in Harvey et al. (2020) and are consistent with those seen in a different cyclone's WCB (Oertel et al. 2020). The case included in this study has been the subject of several recent articles (Maddison et al. 2020, Blanchard et al. 2020), including a recent publications by the authors, and this contribution adds useful new insights to complement the recent research, particularly with the novel observations within the WCB. I thus recommend the article be published subject to minor revisions. I have a couple of broad comments that should be considered before publication and specific and technical comments listed below.

Broad comments:

1) Clarification of online trajectories versus the WCB.

A more careful consideration of how the trajectories shown in the article relate to the WCB ascent would be beneficial. The authors select trajectories in the simulation that ascend 150 hPa in 12 hours (based on the 600 hPa in 48 hour criteria for WCBs used in many other studies). As this is a short time period the trajectories shown don't necessarily correspond to the WCB, as the authors note (section 2.3). As the simulations are run for 36 hours I wonder if there are some trajectories that stay in the domain for longer than 12 hours and could be used to show whether the 12 hour ascents do correspond to part of the WCB or not. Alternatively, successive 12 hour trajectories could be compared in an attempt to "piece together" the WCB flow. This cyclone has been shown to have a WCB (e.g. Maddison et al. 2019) so I would suggest emphasising this (in section 2.3) and terming the ascents "WCB proxy" or something similar. Some properties of the trajectories could then be better explained and would allow for a better placement of the results in the current knowledge. For example, from Figure 7 it appears that the anticyclonic ascents are from the later stages of a WCB ascent (the start at 4km), and the cyclonic ascents from the early part. Also, the characteristic increase and decrease in PV along WCB ascents (e.g. Madonna et al. 2014) is not found here. These should be further explained.
We clarify that the selected ascents "may not all belong to actual WCB trajectories" and refer to Blanchard et al. (2020) for a discussion of the selection criteria. Technically, the scalar tracers used to compute the trajectories are advected during the full 36-h model integration time thus the length of trajectories could be extended. However, the reason for choosing a 12-h window is the domain size, as explained in Section 2.3: "This relatively short time window is chosen to ensure that all relevant trajectories remain in the simulation domain during the 12 h period." (Note that the domain is relatively small compared to earlier WCB studies but still contains 800x800x70 grid points due to the high horizontal resolution.) This is illustrated in Figure 6, where most ascents reaching the red box at the time of observations (11 UTC) are located close to the southern domain boundary at the time of initialization (00 UTC). In particular, the anticyclonic ascents—which "feed" the jet stream core and constitute the WCB outflow—head northward with high velocity at upper levels and their trajectories could be extended by a few hours at most. In contrast, the cyclonic ascents appear to remain longer in the domain but do not contribute to the WCB outflow and jet acceleration thus are not extensively studied here. We clarify that the focus is on the former, especially in Section 5. Finally, the evolution of PV along cyclonic and anticyclonic ascents is further discussed in the text but does not contradict earlier studies (see also response to specific comments).

2) Verification of the simulations against the observations.

Throughout the paper the authors compare the reference and NODIA simulations with each other and with the observations. It would be helpful if the authors included some verifications (e.g. RMSE) to clarify and emphasise the comparisons as it is sometimes difficult to see by eye. I would suggest quantifying the simulations' skill in replicating the observed fields in Figures 1, 2 and 3 (comparing points where observations exist). And also comparing the two simulations with each other in Figures 5 and 8. For example, the authors state that the ridge extends further west in the reference simulation so quantifying this somehow (most westward longitude reached for example) would be helpful as it is a bit confusing because of the complicated structure of the ridges. Also the jet stream maxima should be highlighted in the two simulations and discussed more as the title states that the jet stream is accelerated by the convection in the WCB.
Several metrics have been added to better compare the simulations and assess them against the observations: the Heidke Skill Score is now computed when comparing Meso-NH BTs with BTs measured by MSG (in addition to already comparing the simulated MSLP with the analysis); quantitative statements are included in the comparison of wind speed between RASTA observations and Meso-NH simulations; finally, the bias and the RMSE are given for the comparison between wind speed, potential temperature and relative humidity measured by the dropsondes and simulated by REF and NODIA.

3) Labelling features of interest.

Several features are referred to in the text that are not always easily recognisable among the highly detailed plots. The authors give latitude or longitude points to guide the reader but this can be quite cumbersome. Adding labels (maybe shapes or simply letters) to the plots for some of the features would help with the comprehension of the results. The features mentioned in the text that I would suggest labelling include: the high PV tongue, the tropopause fold, the jet cores, the WCB outflow, the bent back front, the low-level jet and the cloud head. Too many labels can of course obscure features and make the plots more complicated but adding one or two labels to some of the figures when latitude/longitude values are needed in the text would be helpful.
The suggested features of interest are now labeled in maps and vertical cross-sections in Figs. 1, 2, and 3, while references to geographical coordinates have been omitted when unnecessary.

Specific comments:

L22: PV gradients form a waveguide on zonal flows too (without upper-level ridges or troughs), this should be mentioned here. "Zonal flows" are now mentioned.

L86-88: more information on the other parameterisation schemes in the model should be given here. In particular, would other schemes contain heat exchanges within clouds that would still be active in NODIA? We added "Note that the other parameterizations (radiation, turbulence, shallow convection) also exchange heat in the atmosphere, but in a negligible way compared to cloudy processes."

L128: is this a second MSLP centre (were there two?) or just an eastward movement of the cyclone? Evidence should be provided if it is a second MSLP centre development. The evidence of a second MSLP center is given in Fig. 1b in Blanchard et al. (2020). To clarify, the sentence is now "The abrupt shift is due to the creation of a second MSLP center to the east (see MSLP at 16:00 UTC in Fig. 1b in Blanchard et al. (2020)), which therefore has a diabatic origin."

L206: The fact that the observations are well simulated in REF allows for the attribution of features and their development to diabatic processes. This should be emphasised here. Added

L220: What are the ascents over Greenland associated with? We did not investigate the ascents in detail but

their presence in NODIA clearly shows their origin is not diabatic. As explained in the following paragraph "They are likely produced by the combined effect of the warm front dynamics and orographic forcing caused by the Greenland Plateau."

L225-226: I find it surprising that there are almost no ascents in the WCB outflow in NODIA. Is it that the WCB is absent or that the trajectories don't meet the ascent threshold used? It could also be a timing issue in that WCB trajectories may be delayed in NODIA. Would figure 5 look different if a slightly later 12 hour window was chosen? Further explanation should be included here. Indeed they may be trajectories that rise slowly but do not meet the used threshold and thus do not qualify as "ascents" in NODIA. We are actually not surprised as latent heat release associated with cloud diabatic processess—which are switched off in NODIA—are essential to WCB ascents. We added "This absence of trajectories rising by at least 150 hPa in 12 h is consistent with lower cloud tops in NODIA than in REF."

L243: It would be beneficial here if a brief explanation of why/how the anticyclonic trajectories would be expected to impact the upper level flow, via PV modification for example. We added "via injection of low-PV air"

L250-265: can the results be explained here using extratropical cyclone development theory? Does the cyclonic branch of the WCB typically occur later than the anticyclonic? The PV modification along the trajectories is different here than that found in Madonna et al. (2014). There is no increase in PV (as trajectories ascend through heating) and subsequent decrease (as trajectories leave heating). May this have occurred earlier in the ascent? This should be explained here too. The 12-h time window we use for trajectory analysis is too short to compare when the cyclonic and anticyclonic branches of the WCB occur in the Stalactite cyclone, which is beyond the scope of the study. However, for this window, Figure 7 shows that PV actually increases at low levels (cyclonic ascents) and decreases at higher levels (anticyclonic ascents), as expected below and above the diabatic heating maximum along slantwise ascents. This was clarified in the text.

L285: Another feature that is clear in Figure 8 is the PV field is smoother in NODIA. This should be mentioned and explained. We do not fully agree: the PV field shows small-scale features in both NODIA and REF (see the cloud head area for example). The main difference between the two simulations lies in the negative PV bands.

L289: mention that the negative PV bands at 06:00 push the ridge cyclonically to the west as well. We added that they "push the ridge to the west" (and omit "cyclonically" to avoid confusion).

L320-326: Why is there no PV dipole for the strong updraft above 6km altitude? Has the PV signature been dissipated by this time? Please explain this here. This may be due to the weaker vertical wind shear but is rather speculative and not discussed in the paper. However, we note that the absence of a PV dipole happens for the strong updraft above 6 km altitude "that does not meet the criteria for rapid segments", which validates the identification of rapid segments based on pressure difference.

L353: Do heat exchanges still occur in other parameterisations? e.g. cloud scheme? In Sect. 2.2., we added "Note that the other parameterizations (radiation, turbulence, shallow convection) also exchange heat in the atmosphere, but in a negligible way compared to cloudy processes." (see response to l. 86–88)

L383: provide some explanation for the rapid ascending trajectories. Mid-level convection is explained below, while low-level rapid segments occurring along cyclonic ascent are not further studied in the paper.

L388: quantify how much further the ridge extends west in REF. The difference looks quite small. Indeed, the difference is small, but still visible. We added "by about 100 km".

L401: is this region of conditional instability shown? Mention if it is or is not. When we commented on Fig. 9b in Sect. 5, we added "They both lie in a region of vertically homogeneous θ_e values, which promotes conditional instability."

Technical comments:

L3: “structures of negative” should be “structures with negative”. Changed

L6 (and elsewhere): the authors should explain why the cyclone has been given this name. In the abstract this might not be possible so just saying “a cyclone” here and giving the cyclone its name in the main article may be best. We prefer keeping the name in the abstract, because the cyclone has also been described by other authors, and now explain its origin in the text.

L7-9: I would remove the sentence “The observations reveal...” as the abstract is quite long and this isn’t really necessary here. The sentence is crucial to highlight the rare observations and to introduce the double jet stream structure but has been shortened.

L9: change “reproduces well the observed” to “reproduces the observed”. Changed

L15: “near the bent back front” in what? The reference simulation? Yes because anticyclonic ascents are absent in the sensitivity experiment as explained in the previous sentence.

L17: remove “and” before “with the negative”. Removed

L17: thus appear → the convective cells thus appear. Changed

L17: add “the” before “negative PV bands”. Added

L27: reference to Martinez-Alvarado et al. (2018) here. They show Rossby wave amplitude still decreases in more recent NWP model configurations. We now refer to Martinez-Alvarado et al. (2018).

L31-32: change to “WCBs usually flow poleward and upward as coherent...”. Changed

L33: band → bands. Changed

L34: clouds → cloud. Changed

L34: During ascents → During WCB ascent. Changed

L35: which representation is → the representation of which is ... . Changed

L39: impact → impacting. Changed

L50: Add why the cyclone is named stalactite. We added ”The cyclone was named after the low tropopause—which shape was reminiscent of a stalactite—during its intensification phase.”

L106: Add sentence introducing the section and what will be included. We added ”An overview of the cloud structures of the Stalactite cyclone and of the associated upper-level ridge is first given.”

L116: along → above. Changed

L121: structures → structures present. Changed

L125: Change the sentence “REF reproduces well the ...” to “The track of the Stalactite cyclone is well reproduced in REF”. Changed

L128: meridian → meridional. Changed

L145: Highlight where these features are (see broad comment 3). See our response to broad comment 3

L147: 40W until z → 40W, reaching z... . Changed

L149: part → part of the domain. Changed

L158: except on → except in. Changed

L159: eastern part where it → eastern part of the domain where it... . Changed

L159: wind speed values → wind speeds. Changed

L162: simulation completes the description → simulation provides a complete description of... . Changed

L166: number ascents → number of ascents. Changed

L177: profile → profiles. Changed

L183-184: might be worth mentioning that the wind speeds in REF still tend to under-estimate the observed peak wind speeds. We added "with the exception of slightly underestimated peaks.

L248: remove "a" before higher. altitude → altitudes. Changed

L252: remove "a" before strong. Changed

L255: remove the sentence "some start close to the surface". Removed

L265: swap thereafter with "in the following section". Swapped

L270: track → follow. Changed

L281: "the eastern part of the northwestern edge" is confusing to me. Consider rephrasing. The sentence is now: "In NODIA, the northwestern edge of the ridge and the PV tongue are shifted eastward compared to REF (Fig. 8b)."

L287: merge sentences here: NODIA. But → NODIA, but. Merged

L287: DIA → NODIA. Changed

L288: there → here. Changed

L299: what region is shown in Fig 9 a,b? The red box? We have erroneously referred to the brown circles in Fig. 6a. We now refer to the red stars which indicate the position of trajectories closest to the time shown in Fig. 9 a,b.

L327: remove "Thus". Or join to previous paragraph. The paragraph has been attached to the previous one.

L359: is this dry air mass the cyclone's dry intrusion? No, that is why we called it "dry air mass", and not dry intrusion to avoid any misunderstanding.

L361: state what the tropopause fold is at the outer boundary of. Changed to "at the edge of the outer part."

L376: explain or motivate why the focus is on the WCB ascents. The sentence has been removed.

L391: Maddison et al. (2020) seems another appropriate reference to add here. Added

L401: "matches with the organised" → "matches the organised". Changed

L406: PV structures are → PV structure in WCB ascent regions are. Changed

References:

be consistent with journal abbreviations. Checked

L423: page and volume numbers missing. Added

Figures:

Fig1: add 'as' before '(a)'. Added

Fig1: What time are the MSLP contours in (b) and (c) shown? At the same time as the BTs. To avoid confusion, the sentence presenting the MSLP contours is now written in second position.

Fig4: mention that the profiles are shown for both observations and simulations in the caption. Information added

Fig5: if I understand correctly, the red box is used to select WCB outflow ascents? It is a bit confusing as I initially thought all ascents shown had to have passed through the red box at 11:00? Please clarify this in the text or caption. You understand correctly. In the caption of Fig. 5, it is written that "Spatial frequency [(now) number] of air parcels belonging to the ascents fulfilling the ascent criterion" and "the red box [is] the region where the ascents are selected at 11:00 UTC.".

Fig6: 40 trajectories are plotted, out of how many? Give the number in the text or caption. The number of trajectories is 220 000 for anticyclonic ascents and 250 000 for cyclonic ascents). This information is now written in the caption.

REFERENCES:

Oertel, A., Boettcher, M., Joos, H., Sprenger, M., and Wernli, H.: Potential vorticity structure of embedded convection in a warm conveyor belt and its relevance for large-scale dynamics, Weather Clim. Dynam., 1, 127–153, 2020

Maddison, J. W., Gray, S. L., Martínez-Alvarado, O., and Williams, K. D.: Impact of model upgrades on diabatic processes in extratropical cyclones and downstream forecast evolution, Quarterly Journal of the Royal Meteorological Society, 146, 1322–1350, 2020.

Blanchard, N., Pantillon, F., Chaboureau, J.-P., and Delanoë, J.: Organization of convective ascents in a warm conveyor belt, Weather Clim. Dynam., 2020

Maddison, J. W., Gray, S. L., Martínez-Alvarado, O., and Williams, K. D.: Upstream Cyclone Influence on the Predictability of Block Onsets over the Euro-Atlantic Region, Monthly Weather Review, 147, 1277–1296, 2019

Madonna, E.,Wernli, H., Joos, H. and Martius, O. (2014) Warm conveyor belts in the ERA-Interim dataset (1979–2010). Part I: Climatology and potential vorticity evolution. J. Climate, 27, 3–26.

Martínez-Alvarado, O., Maddison, J. W., Gray, S. L. and Williams, K. D. (2018) Atmospheric blocking and upper-level Rossby wave forecast skill dependence on model configuration. Quart. J. Roy. Meteor. Soc., 144, 2165–2181.

We thank the Referee for his/her time and his/her constructive comments. We have complied with most of the proposed changes. In the following, the comments made by the Referee appear in black, while our replies are in blue.

Blanchard et al. present a detailed analysis of convection embedded in a WCB and how this affects the upper-tropospheric flow. The study is based on observations taken during the North Atlantic Waveguide and Downstream Impact Experiment and convection-permitting simulations. A reference simulation (REF) generally agrees with the observations and represents key features such as the WCB outflow, a dry region below this outflow and the cloud head associated with the bent-back warm front. A second simulation is performed with latent heating exchanges due to cloud processes being turned off (NODIA). A comparison of the two simulations reveals that elongated bands of negative PV are missing the the NODIA simulation pointing to their diabatic origin. Indeed, the analysis of trajectories and vertical cross section through the WCB suggests that mid-level convection embedded in the WCB is responsible for generating the bands of negative PV in a vertically sheared environment. This is in line with recent studies by Harvey et al. (2020) and Oertel et al. (2020). The study is well written, the figures are mostly clear and the methods are sound. As the paper confirms recent research using novel observations and a slightly different approach (simulations with latent heat release switched on/off), I recommend the article to be published in WCDD after the following comments have been addressed.

Broad comments

1) The REF and NODIA simulations are compared qualitatively throughout the paper. To my impression it would be helpful if the authors provided quantitative estimates of the differences between the simulations since it is sometimes difficult to spot the differences by eye. As an alternative, difference plots would help the reader to fully appreciate the differences (e.g, Fig. 3, 8) which are discussed in the text.
As also suggested by Referee 1, the Heidke Skill Score is now computed when comparing brightness temperatures simulated by Meso-NH and measured by MSG, quantitative statements are included in the comparison of wind speed between RASTA observations and Meso-NH simulations, while the bias and the root-mean square error are given for the comparison between wind speed, potential temperature and relative humidity measured by the dropsondes and simulated by REF and NODIA.

2) The individual subsections are quite often introduced by describing what is shown in the figures. These descriptions are not necessary since they are also provided in the figure captions. Instead, it would be helpful if the authors described the purpose of each subsection in one to two sentences. This would help to guide the reader through the manuscript.
As suggested, the subsection headers have been rephrased to introduce their topic rather than the figures they describe.

Minor comments

l. 2: Please clarify that ”their” is referring to WCBs and not to ”ridges”. Changed to ”the representation of WCBs”

l. 9: Since the ”mesoscale structures” are mentioned here for the first time. Please specify what the ”mesoscale structures” are. Are these the tropopause fold and the jet stream core? We removed ”mesoscale” as we refer to the ”fine-scale observations of cloud and wind structures acquired with airborne Doppler radar and dropsonde”

l. 22: Also PV gradients along zonal flows form a waveguide. Please include this as well. Included

l. 32: I’d suggest to also cite at least one of the early studies, e.g., by Browning et al. (1973) and Harrold (1973). The study of Harrold (1973) is now cited.

l. 32: Other studies state that WCBs are characterized by ”rapid ascent” (e.g., Eckardt et al. 2004). Compared to deep convection the WCB ascent may be considered as ”slow”. Perhaps specify that the ascent is slow compared to deep convective systems. We removed ”slowly”

l. 36: Please specify what "This" is referring to. Changed to "This source"

l. 40: Consider to use "Accordingly" instead of "Thus" to avoid the use of the same wording in two consecutive sentences. Changed

l. 52: Please provide a reference for the statement "persisted for several weeks". The reference to Schäfler et al. (2018) has been added.

l. 72: Specify here that RASTA is a cloud radar. Added

l. 87: Is it only the latent heat exchange which is set to zero or are there also other diabatic processes set to zero? We added "Note that the other parameterizations (radiation, turbulence, shallow convection) also exchange heat in the atmosphere, but in a negligible way compared to cloudy processes."

l. 91: Why are you defining three 3-D passive tracers at each grid point and not only one tracer per grid point? We added "Three scalar tracers per grid point allow to follow the three dimensional position of each air parcel."

l. 98: According to e.g. Browning et al. (1986), WCBs start to ascend from the planetary boundary layer. In terms of their terminology: Are you really identifying a WCB as it was originally defined or is it convection that is embedded in a slantwise ascending WCB? We do not claim to formally identify a WCB. As stated, "Selected ascents thus do not perform a full ascent from the boundary layer to the upper troposphere". We clarify that they "may not all belong to actual WCB trajectories" and refer to Blanchard et al. (2020) for a discussion.

l. 106: Please specify that it is 2 October 11:00 UTC. Added

l. 107: I assume you are meaning "in the eastern half" of the simulation domain. "East of the simulation domain" would actually be outside the domain in Fig. 1. Corrected

l. 114: In the region of the cyclonically turning WCB the BT is lower than observed by MSG. In contrast, in NODIA the BTs are similar to the observed values. Do you have any hypothesis why this might be the case? Thanks for pointing this. The underestimation of the BTs was an artifact due to the cloud properties that were used to compute the BTs. It has been corrected.

l. 113-121: It would be very helpful if you labeled some of the key features in Fig. 1 (e.g., cloud head, PV tongue). Added

l. 132: Please consider to indicate the flight direction (e.g., as an arrow) in Fig. 1a. Added

l. 141: To my impression the slope also indicates the location of the cold conveyor belt which is located below the cloud shield associated with the WCB. If the authors come to the same conclusion this should be mentioned in the text. We agree and mention this in the text.

l. 147: Consider to replace "until" with "reaching down to". Changed to "reaching"

l. 160: Can the authors comment on whether this low-level jet is also part of the cold conveyor belt? We commented that "The low-level jet likely corresponds to the cold conveyor belt with possible orographic influence."

l. 162: "close to those measured" is a quite qualitative statement. Could you either show a difference plot of the modeled and observed wind speed or provide a quantitative measure such as RMSE? Also showing a scatter plot of observed vs modeled wind speeds could provide a more quantitative estimate of the differences. We prefer to keep focus on the impact of the cloud diabatic impact. However, we added "with a bias of 0.5 m s^{-1} and the root-mean square error of 3.3 m s^{-1}" to provide the reader with a quantitative statement.

l. 165: Consider to remind the reader that you have selected all ascents with w $>$ 0.3 m s^{-1}. Or are you showing air parcels that fulfill the ascent criterion of 150 hPa in 12h? Please clarify. We added "(that fulfill the ascent criterion of 150 hPa in 12 h)".

l. 171: Also here, a quantitative statement on the differences would be very helpful. We added "The maximum value is equal to 38 m s^{-1}, a value lower than the maximum of 42 m s^{-1} obtained for REF."

l. 177: Write "profiles" instead of "profile". Changed

l. 180-209: When comparing observations to modeled values at individual grid points, differences might occur due to minor spatial shifts between simulations and observation. To account for these spatial displacements, I suggest to consider the values at several neighboring grid points and to show their variability in Fig. 4. E.g. showing the median value of the grid points together with the interquartile range could be one way to estimate the sampling uncertainty. As one may expect, the simulated fields are rather smooth compared to observations from radiosondes (see curves on Fig. 4). They show zonal gradients (see Fig. 3) but these precisely allow to assess the horizontal extent of the simulated features. For these reasons, and for the sake of visibility, we prefer to show the simulated values at the nearest grid point only. This further allows us to calculate the bias and root-mean square error between the dropsonde measurements and the simulated values for wind speed, potential temperature and relative humidity.

l. 215: To my impression there are only two regions of high ascent frequency. One is associated with the bent back warm front and the second region can be found over Greenland. So, what is the reason for splitting the ascent along the bent back warm front in two regions? Please explain in the text. We do not share your impression, because the area north of the cyclone does not overlap with the bent-back front. To illustrate this point, we have added "(as shown in Sec. 3.2)" after "It corresponds to the WCB outflow region overflown by the aircraft".

l. 223: How did you investigate whether the ascents are produced by the warm front dynamics or by orographic forcing? We did not investigate their origin in detail but their presence in NODIA clearly shows it is not diabatic. The sentence has been rephrased and is now "They are likely produced by the combined effect of the warm front dynamics and orographic forcing caused by the Greenland Plateau."

l. 233: I assume it is Fig. 6a. Corrected

l. 234: I assume it is Fig. 6b. Corrected

l. 235: I assume it is Figs. 6a,b. Corrected

l. 236: I assume it is Fig. 6a. Corrected

l. 237: I assume it is Fig. 6b. Corrected

l. 239: Correct to Fig. 6a. Corrected

l. 240: Correct to Fig. 6c. Corrected

l. 299: Why are you referring to the brown circles? As far as I understand correctly, the red stars in Fig. 6a indicate the position of trajectories closest to the time shown in Fig. 9. Changed to "red stars"

l. 307: The rapid segments are not only found in regions of high θ_e, but especially in regions with high θ_e gradients. This should be mentioned in the discussion. Added

l. 307 and the following paragraphs: It is not quite clear to me why the focus is on 2 October 2 UTC. The differences between REF and NODIA in terms of upper-tropospheric PV (at 320 K) are considerably larger at 06 UTC. In fact, at 320 K differences in PV at 2 UTC are very difficult to identify. It seems that at 2 UTC the negative PV is mostly located in the mid-troposphere. So, could you comment on the processes leading to the negative PV at 320 K at 06 UTC? Since the differences between REF and NODIA are pronounced at 06 UTC, the negative PV is likely not only a result of isentropic advection. We agree that differences on the 320-K isentropic level are larger at 06 UTC. However, the negative PV bands have already formed and convection has weakened at that time. We clarified the focus on the early hours at the beginning of the Section: "The origin of

the negative PV bands is now investigated in the region where both the anticyclonic ascents start (red stars in Fig. 6a) and the elongated negative PV bands found in the WCB outflow region appear to form (box in Fig. 8e). Furthermore, time evolutions have shown that anticyclonic rapid segments are most numerous during the early simulation hours (see black boxplots in Fig. 7a)."

l. 309: Please provide the coordinates of the rapid segments that are located further southwestward. We added "(around 56° N and 30–31° W)"

l. 310: Please specify that you are referring to the black dots in Fig. 9b after the statement "... along the bent-back front". In line 311, please clarify that you are referring to the shading in Fig. 9b when discussing the vertical wind speeds. Changed following your suggestions.

l. 322: What exactly to you mean by "on the jet stream side". Changed to "facing the jet stream core"

l. 335: Fig. 10b is a vertical cross section from south to north. So, how is it possible to see the "western edge of the cloudy area"? Changed to "southern edge of the cloudy area"

l. 354: Can you quantify a bit how much too low? The sentence is now "...whereas the cloud tops are generally 1 km too low in NODIA."

l. 359: Is this air mass between the warm front and the Greenland plateau really dry? I agree that radar does not detect any precipitation, but I am not convinced that this airmass is dry. Also, it would be interesting to know whether this air mass (especially in the lower troposphere) is the cold conveyor belt of the cyclone. We agree that the cloud radar observation can only infer the absence of clouds. However, dropsondes show relative humidity as low as 20%. The air mass is therefore quite dry. The sentence is now "These observations combined with dropsonde measurements ..."

l. 360: Please explain why the dry air mass is absent. An explanation as in l. 155 would be helpful. We added "(cutting off the diabatic cooling reduces evaporation of frozen hydrometeors under the warm front)".

l. 375: Could you explain why the ascents in the WCB outflow are solely due to cloud diabatic processes and not due to frontal dynamics. I think the statement in its current form is very strong and should be reconsidered carefully. Changed to "ascents in the WCB outflow do not occur in the absence of cloud diabatic processes."

l. 386: To support the statement that especially anticyclonic segments are associated with negative PV: Could you indicate the location of anticyclonic and cyclonic segments in Fig. 9d? At 02:00 UTC, rapid anticyclonic segments are located at around 4 km altitude, while rapid cyclonic segments are almost absent (Fig. 7). The former correspond well to the updrafts and to the negative PV values in Fig. 9, while the (few) latter are located further westward and not shown for the sake of clarity.

l. 390: Schemm et al. (2013) performed idealized moist and dry simulations of a baroclinic wave. Their results, in particular with respect to the northwestern edge of the ridge are very similar to the results of this study. Please consider to reference their work. Added

l. 401: The conditional instability is only mentioned here and in the abstract. Please describe already in the previous Section 5 where exactly the conditional instability can be found. It would be helpful to the reader if the regions of conditional instability were highlighted in the figures or if the latitude longitude coordinates of the unstable regions were provided. In the comment on Fig. 9b in Sect. 5, we added "They both lie in a region of vertically homogeneous θ_e values, which promotes conditional instability."

l. 406: This is somewhat related to my previous comment on l. 307. Comparing the evolution of PV at the 320-K isentropic surface in Fig. 8, I have the impression that the negative PV is not simply advected. If this was the case the PV structure should be very similar in REF and NODIA due to conservation of PV in adiabatic flows (Figs. 8c, d). However, REF is characterized by more negative PV in the northwestern corner of the ridge than NODIA. So this clearly points to non-adiabatic processes. My suggestion is that the statement "these structures are then advected by the upper-level anticyclonic flow into the northwestern edge of the ridge"

should be extended in the sense that also the non-conservative processes are at least mentioned. We agree. As tracking the negative PV structures would require different tools than the Lagrangian trajectories and lies beyond the scope of the study, we simply state that the strcututres are "transported by the anticyclonic flow" into the northwestern edge of the ridge.

l. 411: A reference for the statement that models "struggle to represent updrafts that do not start in the boundary layer" is needed. We now refer to the study of McTaggart-Cowan et al. (2020).

Figures

Fig. 1: Please label at least one isobar of the MSLP field in b) and c). Added

Fig. 5: Please indicate the position of the cyclone center with a marker. This will help the reader to follow the description in Section 4.1. Also, what is the unit of the spatial frequency? Is it simply the total number of air parcels or is it the number of air parcels per area? Please clarify. The position of the cyclone center is now shown with "L" and "spatial frequency" is now "number of air parcels".

Fig. 7: What exactly do mean by "number of rapid segments lies above the average"? Does it mean that it is only shown when more than 50. Change to "above their time average".

Fig. 9: "Updrafts and potential vorticity" is a bit confusing since also other parameters are shown. Please consider to remove or replace the first sentence of the caption. Changed to "Results"

References

Browning, K. A., M. E. Hardman, T. W. Harrold, and C. W. Pardoe, 1973: The structure of rainbands within a mid-latitude depression. Quarterly Journal of the Royal Meteorological Society, 99 (420), 215–231, doi:10.1002/qj.49709942002.

Browning, K. A., 1986: Conceptual Models of Precipitation Systems. Wea. Forecasting, 1, 23–41, https://doi.org/10.1175/1520-0434(1986)001¡0023:CMOPS¿2.0.CO;2.

Eckhardt, S., A. Stohl, H. Wernli, P. James, C. Forster, and N. Spichtinger, 2004: A 15-Year Climatology of Warm Conveyor Belts. J. Climate, 17, 218–237,https://doi.org/10.1175/1520-0442(2004)017¡0218:AYCOWC¿2.0.CO;2.

Harrold, T. W., 1973: Mechanisms influencing the distribution of precipitation within baroclinic disturbances. Quarterly Journal of the Royal Meteorological Society, 99(420), 232–251, doi: 10.1002/qj.49709942003

McTaggart-Cowan, R., Vaillancourt, P. A., Separovic, L., Corvec, S., and Zadra, A., 2020: A Convection Parameterization for Low-CAPE Environments, Mon. Weather Rev., in press, https://doi.org/10.1175/MWR-D-20-0020.1

Schäfler, A., Craig, G., Wernli, H., Arbogast, P., Doyle, J. D., McTaggart-Cowan, R., Methven, J., Rivière, G., Ament, F., Boettcher, M.,Bramberger, M., Cazenave, Q., Cotton, R., Crewell, S., Delanoë, J., Dörnbrack, A., Ehrlich, A., Ewald, F., Fix, A., Grams, C. M., Gray,S. L., Grob, H., Groß, S., Hagen, M., Harvey, B., Hirsch, L., Jacob, M., Kölling, T., Konow, H., Lemmerz, C., Lux, O., Magnusson, L.,Mayer, B., Mech, M., Moore, R., Pelon, J., Quinting, J., Rahm, S., Rapp, M., Rautenhaus, M., Reitebuch, O., Reynolds, C. A., Sodemann,465H., Spengler, T., Vaughan, G., Wendisch, M., Wirth, M., Witschas, B., Wolf, K., and Zinner, T.: The North Atlantic Waveguide andDownstream Impact Experiment, Bull. Amer. Meteo. Soc., 99, 1607–1637, https://doi.org/10.1175/BAMS-D-17-0003.1, 2018

Schemm, S., H. Wernli, and L. Papritz, 2013: Warm Conveyor Belts in Idealized Moist Baroclinic Wave Simulations. J. Atmos. Sci., 70, 627–652, https://doi.org/10.1175/JAS-D-12-0147.1.

Mid-level convection in a warm conveyor belt accelerates the jet stream

Nicolas Blanchard[1], Florian Pantillon[1], Jean-Pierre Chaboureau[1], and Julien Delanoë[2]

[1]Laboratoire d'Aérologie, Université de Toulouse, CNRS, UPS, Toulouse, France
[2]LATMOS/IPSL, UVSQ Université Paris-Saclay, Sorbonne Université, CNRS, Guyancourt, France

Correspondence: Florian Pantillon (florian.pantillon@aero.obs-mip.fr)

Abstract. Jet streams and potential vorticity (PV) gradients along upper-level ridges~~and troughs~~, troughs and zonal flows form a waveguide that governs midlatitude dynamics. Warm conveyor belt (WCB) outflows often inject low-PV air into ridges and ~~their representation~~ the representation of WCBs is seen as a source of uncertainty for downstream forecasts. Recent studies have highlighted the presence of mesoscale structures ~~of~~ with negative PV in WCBs, the impact of which on large-scale dynamics is still debated. Here, fine-scale observations of cloud and wind structures acquired with airborne Doppler radar and dropsondes provide rare information on the WCB outflow of the Stalactite cyclone and the associated upper-level ridge on 2 October 2016 during the North Atlantic Waveguide and Downstream Impact Experiment. The observations ~~reveal~~ show a complex tropopause structure ~~with a high PV tongue separating~~ associated with two jet stream cores along the northwestern edge of the ridge~~in two parts, each with cirrus-type clouds and accompanied by a jet stream core, and bounded by a tropopause fold~~. A reference, convection-permitting simulation with full physics reproduces ~~well the observed mesoscale~~ the observed structures and reveals the presence of elongated negative PV bands along the eastern jet stream core. In contrast, a sensitivity experiment with heat exchanges due to cloud processes cut off shows lower cloud tops, weaker jet stream cores, a ridge less extended westward, and the absence of negative PV bands. A Lagrangian analysis based on online trajectories shows that the anticyclonic branch of the WCB outflow ~~feeds~~ enters the eastern jet stream core in the reference simulation, while it is absent in the sensitivity experiment. The anticyclonic ascents and negative PV bands originate from the same region near the cyclone's bent-back front. The most rapid ascents coincide with mid-level convective cells identified by clustering analysis, which are located in a region of conditional instability below the jet stream core and above a low-level jet. Horizontal PV dipoles are found around these cells ~~and~~ with the negative poles reaching absolute negative values, the convective cells thus appear as the source of the negative PV bands. The results show that mid-level convection within WCBs accelerates the jet stream and may ~~thus~~ influence the downstream large-scale circulation.

1 Introduction

Jet streams and potential vorticity (PV) gradients along upper-level ridges~~and troughs~~ , troughs and zonal flows form a waveguide that governs the propagation of Rossby waves (Hoskins and Ambrizzi, 1993). Rossby waves are the main drivers of mid-latitude dynamics, constrain the formation of surface cyclones and anticyclones and act as precursors to high-impact weather events. An accurate representation of jet streams and PV gradients is therefore crucial in numerical weather prediction systems. However, it has been found that the PV gradient across the tropopause adjacent to ridges and the amplitude of Rossby waves decrease with lead time in global model forecasts until about 5 days ~~(Gray et al., 2014)~~(Gray et al., 2014; Martínez-Alvarado et al., 2018). More recently, it has been shown that analyses and short-term forecasts tend to underestimate the peak jet stream wind, the vertical wind shear and the abruptness of the change in wind shear across the tropopause (Schäfler et al., 2020). This calls for a better understanding of processes controlling PV gradients.

Warm conveyor belt (WCB) outflows are one of the main perturbations to the midlatitude waveguide. WCBs ~~are usually~~ usually flow poleward and upward ~~,~~ as coherent airstreams associated with extratropical cyclones ~~(Wernli and Davies, 1997). Rising slowly~~ (Harrold, 1973; Wernli and Davies, 1997). Rising with rates not exceeding $50\,\mathrm{hPa\,h^{-1}}$, the warm and moist air in WCBs cools and condenses to form ~~a~~ wide, elongated ~~band of clouds~~ bands of cloud where heavy precipitation and strong surface winds occur (Browning, 1999). During WCB ascents, a large amount of latent heating is released by cloud processes, ~~which representation~~ the representation of which is considered a major source of uncertainty (Chagnon et al., 2013; Martínez-Alvarado et al., 2014; Joos and Forbes, 2016). This source can be explained from the PV perspective, where PV is produced below the level of maximum heating and reduced above (Hoskins et al., 1985). In WCBs, vertical PV dipoles are created with positive PV anomalies in the lower layers and negative PV anomalies in the upper layers (Wernli and Davies, 1997). The ~~negative PV anomalies are then advected~~ low-PV air resulting from the negative anomalies is then transported into the upper-level ridge by the WCB outflow~~thus impact the~~ , where it is advected toward high-PV air by the associated divergent wind and impacts both the jet stream and the PV gradient at the tropopause ~~. Thus~~(Grams et al., 2011). Accordingly, errors in the PV change by cloud processes lead to errors at upper levels (e.g. Maddison et al., 2019).

Recent studies have shown the presence of mesoscale negative PV structures in WCBs (Harvey et al., 2020; Oertel et al., 2020; Blanchard et al., 2020). Harvey et al. (2020) developed a theory explaining that diabatic heating in the presence of vertical wind shear results in negative PV values on the equatorward side of the jet stream. Oertel et al. (2020) showed with a composite analysis that convective ascents produce horizontal PV dipoles, which persist for about $10\,\mathrm{h}$ and merge to form elongated negative PV bands that can locally accelerate the jet stream. Blanchard et al. (2020) showed that, among three types of organized convection they found in a WCB region, only mid-level convection is associated with coherent negative PV bands. These studies further suggest that the mesoscale negative PV structures may accelerate the jet stream locally and potentially influence the downstream circulation.

This paper is focused on the WCB outflow of the Stalactite cyclone observed during the North Atlantic Waveguide and Downstream Impact Experiment (NAWDEX; Schäfler et al., 2018). The cyclone was named after the low tropopause—which shape was reminiscent of a stalactite—during its intensification phase. On 2 October 2016 the WCB outflow was sampled with

airborne instruments with the objective to characterize its role in the building of the downstream ridge. Two days later, this ridge became a block over Scandinavia and persisted for several weeks (Schäfler et al., 2018). Previous studies showed the major role of diabatic heating in the Stalactite cyclone's WCB on the subsequent onset of blocking (Maddison et al., 2019, 2020; Steinfeld et al., 2020). Maddison et al. (2019) conducted an ensemble sensitivity analysis in which the Stalactite cyclone is clearly identified as the main feature influencing the block onset 3–4 days ahead. Maddison et al. (2020) showed, through several sensitivity experiments to a convective parameterization in a global model, that stronger latent heating in the WCB leads to a more amplified ridge after 6 days lead time. Steinfeld et al. (2020) found a strong influence of latent heating in the Stalactite cyclone on the ridge building after 2 days of simulations.

The objective of this study is to examine the WCB outflow at fine scale and to investigate the cloud diabatic effects in the WCB during a ~~relative~~ relatively short 12-h window. To achieve this objective, we use the convection-permitting simulation described in Blanchard et al. (2020) and run a second simulation set up in the same manner, except with the diabatic impact of clouds turned off. We compare both simulations with airborne Doppler radar and dropsonde measurements taken in the WCB outflow. After showing the cloud diabatic effects in the northwestern edge of the ridge, we trace them back to mid-level convection that occurs in the western flank of the WCB a few hours earlier.

The paper is structured as follows: Section 2 briefly introduces the observations as well as the model simulations and numerical tools used for the analysis. Section 3 describes in detail the airborne observations of the ridge and WCB outflow. Section 4 characterizes the ascents ending in the WCB outflow by studying their Lagrangian back-trajectories, while distinguishing between those with an anticyclonic and a cyclonic curvature. Section 5 focuses on the origin of PV structures in the observed regions before discussing the link with mid-level convective ascents within the WCB. Section 6 concludes the paper.

2 Data and methods

2.1 Airborne observations

Cloud radar RASTA (RAdar Airborne System; Delanoë et al., 2013) and dropsonde observations were acquired from the SAFIRE (Service des Avions Français Instrumentés pour la Recherche en Environnement) Falcon 20 based on Keflavik, Iceland. On the morning of 2 October 2016, the Falcon 20 flew toward Greenland with the objective of studying the tropopause structure and the WCB outflow from the Stalactite cyclone ~~(flight 6, Schäfler et al., 2018, see the track in Fig. 1a.)~~(flight 6 in Schäfler et al., During its cruise, the aircraft flew at around 10 km altitude. On its way back to Iceland, four Vaisala RD94 dropsondes were launched at 10:26, 10:32, 10:36 and 10:41 UTC. In the following, we will discuss the profiles of wind speed, potential temperature and relative humidity (with respect to liquid water below the melting level and to ice above) obtained from the dropsondes as well as the reflectivity and wind speed obtained from ~~the cloud radar~~ RASTA between 10:25 and 11:27 UTC, hereinafter referred to as the 11:00 UTC leg. The reader is referred to Blanchard et al. (2020) and the references therein for more details on RASTA operated on 2 October.

2.2 Meso-NH convection-permitting simulations

Two simulations, REF and NODIA, were performed with the version 5.3 of the non-hydrostatic mesoscale atmospheric Meso-NH model (Lac et al., 2018) over the domain shown in Fig. 1. Both simulations are convection permitting with a grid spacing of 2.5 km horizontally and vertically from 60 m near the surface to 600 m in the upper levels. They are run from 00:00 UTC, 2 October 2016 to 12:00 UTC, 3 October with hourly outputs and initial and boundary conditions provided by the ECMWF (European Centre for Medium-Range Weather Forecasts) operational analyses. Both simulations share the same parameterizations, differing only in that the heat exchanges in the cloud microphysical scheme are set to zero in NODIA. Note that the other parameterizations (radiation, turbulence, shallow convection) also exchange heat in the atmosphere, but in a negligible way compared to cloud processes. The REF simulation is described in Blanchard et al. (2020), where more details are given on the parameterizations as well as on radiative tools used to emulate the RASTA and Meteosat Second Generation satellite (MSG) observations. Following Söhne et al. (2008) we compare synthetic and satellite observations to compute the categorical Heidke skill score (HSS), which measures the fraction of correct forecasts after eliminating those that would be correct by chance.

2.3 Lagrangian trajectory and clustering tools

Lagrangian trajectories are calculated online by ~~defining three 3-D~~ initializing passive tracers at each grid point in the simulation domain (Gheusi and Stein, 2002). Three scalar tracers per grid point allow to follow the three dimensional position of each air parcel. These tracers are advected by the piecewise parabolic method scheme (Colella and Woodward, 1984), known to conserve well the mass properties of the tracers with a weak numerical diffusion. Back-trajectories are reconstructed from the tracers and are studied for the period from 00:00 until 12:00 UTC on 2 October. This relatively short time window is chosen to ensure that all relevant trajectories remain in the simulation domain during the 12 h period. As in Blanchard et al. (2020), trajectories rising by at least 150 hPa in 12 h are defined as ascents. This threshold is based on the usual criterion of 600 hPa in 48 h used to identify WCB trajectories (e.g., Wernli and Davies, 1997; Martínez-Alvarado et al., 2014; Oertel et al., 2020) but without any constraint on the initial altitude of the trajectories, in contrast with previous studies. Selected ascents thus do not perform a full ascent from the boundary layer to the upper troposphere and may not all belong to actual WCB trajectories (see Blanchard et al., 2020, for a discussion).

Coherent structures within the WCB are detected with the clustering tool created and implemented in Meso-NH by Dauhut et al. (2016). Coherent updraft structures consist of 3-D objects made of connected grid points for which the vertical velocity is higher than a threshold of $0.3\,\mathrm{m\,s^{-1}}$ as in Blanchard et al. (2020). In the same way, coherent negative PV structures are defined as areas of connected grid points with PV values lower than $-1\,\mathrm{PVU}$ ($1\,\mathrm{PVU} = 10^{-6}\,\mathrm{K\,kg^{-1}\,m^2\,s^{-1}}$).

3 Observations of the upper-level ridge at 11:00 UTC

3.1 Overview

An overview of the cloud structures of the Stalactite cyclone and of the associated upper-level ridge is first given. At 11:00 UTC 2 October, the Stalactite cyclone approached Iceland as shown by the infrared MSG brightness temperature (BT, Fig. 1a). The elongated band of primarily high clouds observed ~~east~~ in the southeastern part of the simulation domain (BT values less than $-35°$ C) locates the WCB ascent region. High clouds are also present ~~north and partly southwest~~ in the northern and partly southwestern parts of the domain and indicate the WCB outflow and cloud head regions, respectively. Mid-level clouds are also detected in these regions (BT values between $-35°$ and $0°$ C). Positive BT values locate the dry intrusion between the cloud head and WCB ascent regions. Some isolated low-level clouds are observed below the dry intrusion. The aircraft crossed the WCB outflow region when flying back to Keflavik during the 11:00 UTC leg.

In REF, the position of the main cloud structures is correctly reproduced although high clouds are more spatially extended in the cloud head and WCB regions (Fig. 1b). The smoothed 2 PVU contour at the 320 K level (blue line) shows that the upper-level ridge, defined as the low PV region, covers the northeast three quarters of the domain. It also highlights a complex PV structure over the cloud head and ~~along~~ above the Greenland coast. North of 60° N, a tongue of high PV value with relatively ~~lower~~ low cloud tops cuts the northwestern edge of the ridge in two parts.

In NODIA, the main cloud structures are also reproduced but with higher BT values than in the MSG observation and REF in the cloud head and WCB regions (Fig. 1c). Cloud tops are therefore expected to be lower in these regions. However, the Heidke skill score for BT values below $-35°$ C is similar for both simulations when compared to MSG (0.7), which shows that the general pattern of high clouds is not strongly impacted in NODIA. Note that the dry intrusion extends less to the northwest. The 2 PVU contour shows a pattern similar to REF, but with the PV tongue shifted eastward and less small-scale structures present.

The location of the mean sea level pressure (MSLP) minimum of the Stalactite cyclone, represented by the red dotted lines during the simulated 36 h period, shows that the cyclone moves northward on the morning of 2 October. In the ECMWF analysis (Fig. 1a), an abrupt eastward shift then occurs between 12:00 UTC, 2 October and 00:00 UTC, 3 October as the cyclone deepens and finally moves northwestward towards the Greenland Plateau. ~~REF reproduces well the~~ The track of the Stalactite cyclone is well reproduced in REF, including the abrupt eastward shift, as well as its deepening from 968 to around 955 hPa (Fig. 1b). In NODIA, the MSLP minimum values are higher by ∼5 hPa compared to ECMWF and REF (Fig. 1c). ~~The~~ In addition, the abrupt eastward shift is not reproduced, resulting in a more ~~meridian~~ meridional cyclone track. The abrupt shift is due to the creation of a second MSLP center to the east ~~therefore has a diabatic origin (see the second MSLP center~~ (see MSLP at 16:00 UTC in Fig. 1b in Blanchard et al. (2020)), which therefore has a diabatic origin.

3.2 Vertical structure of the upper-level ridge across the flight leg

In the following, we focus on the WCB outflow region overflown by the Falcon 20 aircraft along the 11:00 UTC leg. Its track is indicated by the black lines in Fig. 1a, while the location of the dropsondes launched during the flight are marked by white stars. The observations of the RASTA radar and the dropsondes, combined with the REF results, provide a fine-scale description of the upper-level dynamics in the region.

The vertical structure of reflectivity as seen by RASTA shows a large cloud system between ~~40~~43.5° and 27° W (Fig. 2a). Weak reflectivity values (about $-20\,\mathrm{dBZ}$) are measured above $\approx 7\,\mathrm{km}$ altitude. These values are characteristic of cirrus-type clouds. Their location is consistent with strong negative BT values shown in Fig. 1a. Reflectivity values then increase below z$\approx$7 km. Reflectivity values of $10\,\mathrm{dBZ}$ are measured in the first kilometer of altitude with local peaks greater than $15\,\mathrm{dBZ}$ at z$\approx$1 km highlighting the melting level. They are lower between 1 and $\approx 7\,\mathrm{km}$ altitude with local peaks of $10\,\mathrm{dBZ}$. The slope in the vertical structure of reflectivity between 40° and 35.5° W reveals the warm front associated with the cyclone and indicates the location of the cold conveyor belt. Isolated convective structures, highlighted by the reflectivity values greater than $15\,\mathrm{dBZ}$, are present below ~~the slope of the warm front~~ around 39° and 37° W as well as above the Greenland Plateau around 42° W. The lack of radar signal (lower than $-20\,\mathrm{dBZ}$) between the warm front slope and the isolated convective structures suggests the presence of a dry air mass. This dry air mass in the mid levels is hardly detectable on the BT field in Fig. 1a.

The WCB outflow region, the slope of the warm front, the isolated convective structures and the dry air mass are well reproduced by REF with reflectivity values similar to those observed (Fig. 2b). The 2 PVU contour shows the PV tongue between 37°–38° W which penetrates the troposphere down to z$\approx$8 km. It also reveals a tropopause fold west of 40° W ~~until~~ reaching z$\approx$6 km, which covers the upper part of the dry air mass. Note the spots of negative PV at the tropopause ~~on~~ in the eastern part of the domain. In NODIA, the vertical structure of reflectivity shows higher values around the melting level and mid levels compared to the RASTA observation and REF (Fig. 2c). This can be explained by higher contents of frozen hydrometeors (graupel and snow at the melting level and mid levels, respectively) due to the cut-off of diabatic heating from cloud processes. The upper levels are also impacted. The level of the cloud top ~~on~~ in the eastern part does not exceed $\approx 7\,\mathrm{km}$ altitude while it is higher than z=8 km in the observation and REF. Moreover, the tropopause fold and the PV tongue are shifted eastward compared to those simulated in REF. Finally, the dry air mass is not reproduced in NODIA. This can be explained by a lower evaporation of frozen hydrometeors under the warm slope due to the cut-off of diabatic cooling from cloud processes.

The vertical structure of the horizontal wind speed measured by RASTA shows in part the jet stream with values greater than $25\,\mathrm{m\,s^{-1}}$ above z$\approx$7 km (in yellow in Fig. 3a). Local peaks of $40\,\mathrm{m\,s^{-1}}$ are measured in the upper levels (in red). The horizontal wind speed decreases below. It is quite homogeneous in the middle and low levels (around $10\,\mathrm{m\,s^{-1}}$) except ~~on~~ in the eastern part of the domain where it reaches $20\,\mathrm{m\,s^{-1}}$ between 2 and 6 km altitude. Horizontal wind ~~speed values~~ speeds greater than $25\,\mathrm{m\,s^{-1}}$ below z=2 km around 42° W and 39° W show the presence of a low-level jet along the Greenland coast. The low-level jet likely corresponds to the cold conveyor belt with possible orographic influence.

The vertical structure of the horizontal wind speed in the WCB outflow region is well reproduced by REF with horizontal wind speed values close to those measured, with a bias of $0.5\,\mathrm{m\,s^{-1}}$ and a root-mean square error of $3.3\,\mathrm{m\,s^{-1}}$ (Fig. 3b). The simulation ~~completes the~~ provides a complete description of the jet stream and reveals two intensity maxima, hereafter called jet stream cores. The first is located at z$\approx$8 km between 43° and 40° W and the second at z$\approx$9 km between 37° and 31° W. The value of the horizontal wind speed in these two cores locally exceeds $40\,\mathrm{m\,s^{-1}}$ (in red). The low-level jet is also well reproduced in REF. The black dots show the position of the selected ascents ~~in~~ (that fulfill the ascent criterion of 150 hPa in 12 h) in the cross section at 11:00 UTC. A large number of ascents are located above the Greenland Plateau and the low-level jet. Many ascents are also located in the cloudy area, mainly in the eastern part. They are separated in two distinct layers. Most are located

in the upper layers, between ≈4 and 10 km altitude, within regions of large wind speed ~~. They feed~~ corresponding to the eastern jet stream core. The other ascents are located in the lower layers, below z=4 km altitude, near regions of high reflectivity. In NODIA, the jet stream and the low-level jet are both less intense, (Fig. 3c). The maximum value is equal to 38 $\mathrm{m\,s^{-1}}$, a value lower than the maximum of 42 $\mathrm{m\,s^{-1}}$ obtained for REF. The western jet stream core is less spatially extended while the eastern jet stream core is shifted eastward. Thus, cloud diabatic processes strengthen the jet stream and modify its location in this case. In NODIA, only the ascents above the Greenland Plateau and the low-level jet are present. They are not studied afterwards in order to focus on the ascents of diabatic origin in REF.

3.3 Analysis of the western jet stream core

The ~~vertical profiles of horizontal wind speed, potential temperature (θ) and relative humidity (RH), measured by~~ western jet stream core and its representation in simulations are further investigated with help of the four dropsondes launched along the 11:00 UTC leg (see Fig. 1a)~~,~~. The vertical profiles of horizontal wind speed, potential temperature (θ) and relative humidity (RH) are shown in Fig. 4 ~~a–d, Fig. 4e–h and Fig. 4i–l, respectively (black lines).~~ from west to east. The two westernmost dropsondes (at 43.3° and 41.8° W) were launched over the Greenland Plateau, so their ~~profile~~ profiles stop at an altitude close to 2 km. The other two dropsondes (at 40.7° and 39.2° W) were launched along the Greenland coast, over the western edge of the cloudy area. ~~The profiles from REF and NODIA are superimposed on those observed.~~

The horizontal wind speed profile measured at 43.3° W shows a peak of ≈35 $\mathrm{m\,s^{-1}}$ at z=8 km (black line in Fig.4a). At 41.8° and 40.7° W, the horizontal wind speed reaches 42 $\mathrm{m\,s^{-1}}$ and extends vertically from 8 to 10 km altitude (black lines in Fig.4b,c). At 39.2° W, it peaks again at 35 $\mathrm{m\,s^{-1}}$ at these heights (black line in Fig.4d). This zonal variation validates the existence of the simulated western jet stream core seen in Fig. 3b. Its height and intensity are well reproduced by REF, though slightly underestimated peaks (red lines in Fig.4a–d)~~but~~, while it is slower by up to ≈10 $\mathrm{m\,s^{-1}}$ in NODIA (orange lines in Fig.4a–d). Below the jet stream, the horizontal wind speed decreases down to z≈7 km at the western dropsonde location and z≈5 km at the eastern dropsonde location, in both observation and simulations. The horizontal wind speed then varies from 5 to 20 $\mathrm{m\,s^{-1}}$ until z≈2 km. A second peak of horizontal wind speed of 25 $\mathrm{m\,s^{-1}}$ is measured in the lower troposphere by the two easternmost dropsondes (around z=2 km in Fig. 4c and z=1 km in Fig. 4d). This corresponds to the presence of the low-level jet described in Fig. 3a. The low-level jet is also well reproduced in the two simulations (red and orange lines in Fig. 4c,d) albeit one kilometer lower. Overall, the bias ± the root-mean square error is -0.4 ± 5.1 $\mathrm{m\,s^{-1}}$ for REF and -0.7 ± 5.6 $\mathrm{m\,s^{-1}}$ for NODIA.

The measured θ profiles show a slight increase with altitude from ≈280 K in the lower levels to ≈300 K at z=6 km (black lines in Fig. 4e–h). At 43.3° W, θ increases sharply above to reach 325 K at z=9 km (Fig. 4e). This layer of high increase in θ corresponds to the location of the tropopause fold. This is well reproduced by the simulations (red and orange lines in Fig. 4e). At 41.8° and 40.7° W, θ slightly increases from z≈7 km before increasing abruptly again at z≈9.5 km, both in observations and simulations (Fig. 4f,g). This indicates the presence of a second tropopause level, in addition to the one located at z≈6 km. This is consistent with the locations of the simulated stratospheric PV values and the dynamical tropopause height at the location of the dropsondes. At 39.2° W, θ increases slightly up to 330 K at z≈9.5 km before increasing suddenly above

(Fig. 4h). This altitude corresponds to the dynamical tropopause height at the location of the dropsonde and is also reproduced by the simulations. The bias $\pm$ the root-mean square error is 1.7 ± 2.2 K for REF and -0.6 ± 2.4 K for NODIA.

The RH profile at 43.3° W shows values of less than 20% above 7 km altitude in both observation and simulations (Fig. 4i). This confirms the absence of high clouds on the western edge of the cross-section. Below, RH reaches larger values, up to 100% and more, at z=4 km. This highlights the location of mid-level clouds over the Greenland Plateau. The measured supersaturation is not reproduced by the simulations because of ~~the~~ a saturation adjustment in the microphysical scheme. The RH profiles of the other three dropsondes show high values (close to 100%) above z=7 km (Fig. 4j,k,l). They correspond to the cirrus-type clouds observed in Fig. 2a. A sharp decrease in RH (from 100 to 20%) is measured between ≈5<z<7 km, ≈4<z<7 km and ≈3<z<6 km at 41.8°, 40.7° and 39.2° W, respectively. This is consistent with the location of the dry air mass observed by RASTA and simulated in REF. This decrease in RH is not reproduced in NODIA, which matches the absence of dry air mass in Fig. 2c. The fact that the observations are well simulated in REF and not in NODIA allows for the attribution of features to diabatic processes. Below the dry air mass, the RH show values close to 100%, referring to isolated convective structures along the Greenland coast in Fig. 2a,b. The bias $\pm$ the root-mean square error is 3.5 ± 18.6% for REF and 13.2 ± 26.7% for NODIA. Overall, the measured vertical profiles complement the RASTA observations and are consistent with the vertical structures simulated in REF.

4 Evolution of ascents in the WCB outflow

4.1 Selection of ascents

~~The location of air parcels respecting~~ To investigate the dynamics of simulated trajectories belonging to the WCB outflow, air parcels are first selected if they respect the ascent criterion of 150 hPa between 00:00 and 12:00 UTC, 2 October~~is shown~~. Their location is compared at 11:00 UTC ~~for REF (Fig. 5a)~~ between REF and NODIA (Fig. 5~~b). The colored contours represent the equivalent potential temperature θ_e at z≈1 altitude at 11:00 UTC.~~).

In REF, three regions of high ascent ~~frequency~~ number are highlighted (in blue and green in Fig. 5a). The first region is located to the north of the cyclone center ~~, above high θ_e values. It~~ and corresponds to the WCB outflow region overflown by the aircraft ~~.~~ (as shown in Sec. 3.2). The red box is used as a mask to select the ascents located there at 11:00 UTC. The second region is located ~~southwest~~ in the southwestern part of the domain ~~, between 53–61 N and 40–25 W. It~~ and is associated with the cloud head region. The tightening of iso-θ_e contours in this region shows the winding of the bent-back front around the cyclonic center, where some local peaks of high ascent ~~frequency~~ number are located. Some ascents are identified further westward. The third region is located ~~northwest~~ in the northwestern part of the domain, above Greenland.

In NODIA, only two regions of high ascent ~~frequency~~ number are highlighted: Greenland and the bent-back front region (Fig. 5b). Thus, ascents in these two regions have a dynamic origin. Those above Greenland are as numerous as in REF ~~. They are~~ and are likely produced by the combined effect of the warm front dynamics and orographic forcing caused by the Greenland Plateau. A higher ~~frequency~~ number of ascents is even identified compared to REF along the bent-back front, between 54°–56° N and 35°–30° W. In contrast, ascents are almost lacking in the WCB outflow region (red box), which indicates their

diabatic origin. This absence of trajectories rising by at least 150 hPa in 12 h is consistent with lower cloud tops in NODIA than in REF. In the following, only ascents from this region are further discussed.

4.2 Location of the selected ascents

The ascents simulated by REF in the WCB outflow region at 11:00 UTC are now examined. ~~An overview is presented in Fig. 6 by showing a sample of their trajectories colored by altitude between 00~~Anticyclonic trajectories are distinguished from cyclonic trajectories based on their curvature between 06:00 UTC and 12:00 UTC. ~~For better visibility, anticyclonic trajectories (~~An overview is presented in Fig. 6 ~~a) are distinguished from cyclonic trajectories (Fig. 6b). Cyclonic (anticyclonic) trajectories are identified based on their cyclonic (anticyclonic) curvature between 06~~by showing samples colored by altitude between 00:00 UTC and 12:00 UTC.

At 00:00 UTC, most anticyclonic ascents are located along a band extending from ≈56° N and ≈30° W to ≈53° N and ≈22° W (red stars in Fig. ~~5~~6a). Their position corresponds to the location of the bent-back front at this time (not shown). The majority of cyclonic ascents also starts along this band, while some start further north (red stars in Fig. ~~5~~6b). At 06:00 UTC, all the ascents have been advected northward by the large-scale flow (black dots in Fig. ~~5~~6a,b). Most of the anticyclonic ascents end in the eastern part of the 11:00 UTC leg (brown circles in Fig. ~~5~~6a). A few of them end further north. Some cyclonic ascents also end in the eastern part of the 11:00 UTC leg but the majority end further south (brown circles in Fig. ~~5~~6b).

The anticyclonic ascents are higher in altitude than the cyclonic ascents. They are located between ≈4000<z<7000 m at 00:00 UTC (in light blue and green in Fig. ~~5~~6a) and ≈7000<z<10000 m at 12:00 UTC (in orange). In contrast, the cyclonic ascents remain below z≈5000 m between 00:00 UTC and 12:00 UTC (in blue in Fig. ~~5~~6c). Thus, the anticyclonic ascents correspond to the ascents found at 11:00 UTC in the eastern jet stream core (Fig. 3b) and the cyclonic ascents to those found in the lower layers. The ascents with an anticyclonic curvature are similar to the anticyclonic branch of the WCB (Martínez-Alvarado et al., 2014). They are therefore expected to impact the upper-level ridge via injection of low-PV air in the WCB outflow region.

4.3 Properties of the selected ascents

The ~~temporal evolution of altitude and PV~~ anticyclonic and cyclonic trajectories are further investigated with help of time evolutions along the selected ascents ~~simulated in REFis examined (Fig. 7).~~ in REF. The 2 h part of the trajectories which undergo an ascent greater than 100 hPa are also discussed ~~. They~~ and are referred to as rapid segments thereafter. Overall, there are about as many anticyclonic ascents (53%) as there are cyclonic ascents (47%).

As ~~expected~~already illustrated, anticyclonic ascents are ~~at a higher altitude~~ located at higher altitudes than cyclonic ascents (Fig. 7a). The interquartile ranges (shaded color) do not overlap. The anticyclonic ascents (in blue) are located at z≈4 km at 00:00 UTC and rise continuously until z≈7 km at 12:00 UTC, on average. Some exceed z=8 km at the end of the trajectory. Anticyclonic rapid segments are more numerous at the beginning of the trajectories and take place around z=4 km (black boxplots in Fig. 7a). Their number then decrease with time. This suggests ~~a~~ strong mid-level convective activity in the first hours of simulation, close to the region identified as red stars at 00:00 UTC in Fig. 6a. The cyclonic ascents (in orange) are

located at z≈1 km at 00:00 UTC, on average. Contrary to the anticyclonic ascents, they stay at ~~the same~~ similar altitude until 04:00 UTC before rising to z≈3 km (on average) at 12:00 UTC. ~~Some start close to the surface.~~ The cyclonic rapid segments occur later than the anticyclonic rapid segments (red boxplots in Fig. 7a). They are also located at lower altitudes, around z=2 km. This suggests the presence of shallow convective activity at that time.

Potential vorticity decreases slowly along the anticyclonic ascents with PV values ranging from 0.6 PVU at 00:00 UTC to 0.4 PVU at 12:00 UTC on average (Fig. 7b). The interquartile range shows PV values reaching 1.2 PVU at 02:00 UTC and 0.0 PVU during the 12 h period (shaded blue). In contrast, the averaged PV value along the cyclonic ascents first remains around 0.3 PVU then increases between 04:00 UTC and 08:00 UTC when the rapid cyclonic segments occur. As for the anticyclonic ascents, the interquartile range shows PV values between 0.0 PVU and 1.2 PVU (shaded orange). This contrasting PV evolution between ~~upper and lower~~ lower and upper levels of the troposphere corresponds to the classical view of Wernli and Davies (1997) for slantwise ascents, where PV increases below the diabatic heating maximum and decreases above. However, ~~rapid segments, in particular anticyclonic ones, indicate~~ an increasing fraction of rapid segments—in particular anticyclonic ones—indicate negative PV values from 03:00 UTC onward. This suggests that ~~convection, especially at mid levels, is~~ convection—especially occurring at mid levels—is associated with negative PV creation. The origin of this process is detailed ~~thereafter~~in the following section, which thus focuses on convective anticyclonic ascents.

5 Origin of updrafts and negative PV

5.1 Negative PV bands at upper levels

The ~~ridge associated with the Stalactite cyclone is examined~~ region of the ridge that was observed at 11:00 UTC ~~on maps of PV and horizontal wind at~~ is followed back in time on the θ=320 K ~~level in~~ isentropic level and compared between REF and NODIA ~~(Fig. 8a and Fig. 8b, respectively). The same maps are shown at 06:00 UTC (Fig. 8c,d) and at 02:00 UTC (Fig. 8e,f) in order to track~~ to investigate the evolution of ~~the ridge back in time in both simulations.~~ differences between the simulations. PV values larger and smaller than 2 PVU ~~at θ=320~~indicate stratospheric and tropospheric air, respectively (white and color shading in Fig. ~~K show stratospheric air (in white) and PV values lower than 2 tropospheric air(in colors).The~~ 8), while the jet stream follows the tropopause where the PV gradient is strongest (red arrows).

At 11:00 UTC, the ridge in REF largely covers the northeastern part of the domain (Fig. 8a). Above the Greenland Plateau, stratospheric air corresponds to the upper part of the tropopause fold, as shown in Fig. 2b. Further east, the PV tongue with stratospheric air ~~is located between ≈38–35 W around 64 N. It~~ cuts the northwestern edge of the ridge in two parts where the horizontal wind speeds exceed 45 $\mathrm{m\,s^{-1}}$, corresponding to the two jet stream cores described in Fig. 3b. ~~In the eastern part, elongated~~ Elongated negative PV bands (in blue) are simulated ~~between 62–66 N and 35–25 W. This region~~ in the eastern part, in a region that coincides with the location of upper-level anticyclonic ascents (see brown circles in Fig. 6a). A second region with elongated negative PV bands is simulated further south ~~,~~ along another jet stream core (between 54°–58° N and 22°–15° W~~, along another jet stream core~~). This second region was overflown at 16:00 UTC by the Falcon 20 aircraft and is further described in Blanchard et al. (2020).

In NODIA, the ~~PV tongue is~~ northwestern edge of the ridge and the PV tongue are shifted eastward compared to REF (Fig. 8b). The ~~eastern part of the northwestern edge of the ridge is also shifted eastward. The~~ negative PV bands are not reproduced by NODIA, neither in this region nor in the second region further south. This reveals that the elongated negative PV bands are created by cloud diabatic processes. The wind speed is less intense in the two jet stream cores, as already shown in Fig. 3c. Following the ridge, the jet stream is also less curved to the west.

At 06:00 UTC, the ridge is located further south in the domain (Fig. 8c,d). Its western part extends until 40° W in both REF and NODIA~~. But~~, but the part to the east of the PV tongue extends further west ~~around 60 N~~ in REF compared to ~~DIA~~NODIA. The elongated negative PV bands in REF are more concentrated ~~there~~ here than at 11:00 UTC and push the ridge to the west. Once again, they are not reproduced in NODIA and the jet stream is less intense than in REF. At 02:00 UTC, the ridge does not differ much between the two simulations (Fig. 8e,f). This is understandable, as this time is close to the initialization of the simulations, and means the cloud diabatic processes have not yet strongly influenced the upper-level dynamics. In particular, negative PV structures are found in both simulations at that time, and are already present in the initial conditions (not shown).

Overall, the comparison between REF and NODIA shows the impact of cloud diabatic processes that occurred in the WCB on the upper-level dynamics. These processes create negative PV bands that persist over time and are found at the northwestern edge of the ridge at the time of observations. The negative PV bands reinforce the PV gradient at the tropopause level and thus the jet stream.

5.2 Origin of the negative PV bands

The origin of the negative PV bands is now investigated ~~. Firstly, rapid segments along anticyclonic ascents are examined at 02:00 UTC in REF (Fig. 9a,b). Their location corresponds to the region of origin of~~ in the region where both the anticyclonic ascents ~~(brown circles~~ start (red stars in Fig. 6a) and the elongated negative PV bands found in the WCB outflow region ~~(~~appear to form (box in Fig. 8e). Furthermore, time evolutions have shown that anticyclonic rapid segments are most numerous during the early simulation hours (see black boxplots in Fig. 7a). ~~Secondly,~~ Firstly, at 02:00 UTC in REF, rapid segments are examined along anticyclonic ascents, while the creation of negative PV ~~at upper levels~~ is assessed at ~~the same time by showing the negative PV structures and their altitude~~ upper levels (Fig. 9~~c, d~~). Secondly, the results are compared with those of NODIA to highlight the impact of cloud diabatic processes on upper-level dynamics (Fig. 10). For easier interpretation, only coherent negative PV structures are discussed here ~~. They~~ and are defined as ~~regions~~ objects with PV values less than $-1\,\mathrm{PVU}$. ~~The~~ Using the same clustering approach~~is used to identify the base of coherent updrafts , defined as regions~~ , coherent updrafts are identified as objects with vertical wind speed values greater than $0.3\,\mathrm{m\,s^{-1}}$. ~~Finally, the results are compared with those of NODIA to highlight the impact of cloud diabatic processes on upper-level dynamics (Fig. 10).~~

Most anticyclonic rapid segments in REF are located along the bent-back front, above a region of high θ_e values and with high θ_e gradients, at 02:00 UTC (black dots in Fig. 9a). Similarly, coherent updrafts are located along the bent-back front at lower and mid levels (shading). Some anticyclonic rapid segments are also located further southwestward (around 56° N and 30–31° W) but are less numerous and not discussed here. A meridionally oriented vertical cross-section illustrates that anticyclonic rapid segments are mainly located between $\approx 1\,\mathrm{km}$ and $\approx 4\,\mathrm{km}$ altitude along the bent-back front (black dots in

Fig. 9b), where vertical wind speeds from $0.1\,\mathrm{m\,s^{-1}}$ to $0.5\,\mathrm{m\,s^{-1}}$ are simulated (~~black dots~~ shading in Fig. 9b). These ascents correspond to the lower-levels updrafts in Fig. 9a and originate from the frontal uprising, highlighted by the tightening of iso-θ_e contours in the lower layers (black lines in Fig. 9b). Anticyclonic rapids ascents are also identified at higher altitude within two convective cells of vertical velocity ~~greater than 0.9~~close to 1 $\mathrm{m\,s^{-1}}$. The first cell is located between $4\,\mathrm{km}$ and $\approx 7\,\mathrm{km}$ altitude around 56.5° N and the second between $4\,\mathrm{km}$ and $\approx 6\,\mathrm{km}$ altitude around 57° N. They both lie in a region of vertically homogeneous $theta_e$ values, which promotes conditional instability. These mid-level convective cells correspond to the mid-level updrafts in Fig. 9a. A third cell of relatively high vertical wind speed is located between $6\,\mathrm{km}$ and $\approx 9.5\,\mathrm{km}$ altitude around 57° N (Fig. 9b) but it does not ~~match~~ meet the criteria of 100 hPa in 2 h for rapid segments (see Blanchard et al., 2020, for a discussion). ~~These mid-level convective cells correspond to the mid-level updrafts in Fig. 9a.~~

The top altitude of negative PV structures is shown at 02:00 UTC in Fig. 9c (shading) along with the jet stream (black lines). The location of negative PV structures is consistent with updrafts and anticyclonic rapid segments at 02:00 UTC, which follow the eastern edge of the jet stream at upper levels and the bent-back front at lower levels. The vertical cross-section reveals the presence of mesoscale horizontal PV dipoles around the first and second mid-level convective cells (Fig. 9d). They are located above a low-level jet and below the upper-level jet stream. The negative PV poles are ~~on~~ facing the jet stream ~~side~~ core and reach values lower than $-2\,\mathrm{PVU}$, while the positive PV poles reach values larger than $2\,\mathrm{PVU}$. This description is coherent with the findings of Oertel et al. (2020) and Blanchard et al. (2020). Note the absence of a PV dipole for the strong updraft above 6 km altitude that does not meet the criteria for rapid segments. Strong positive PV values are also visible in the low-level jet, below the anticyclonic rapid segments. This corresponds to the classical view of Wernli and Davies (1997), i.e., a vertical PV dipole with positive anomaly below the maximum level of diabatic heating.

~~Thus, the anticyclonic rapid segments that end in the WCB outflow region at 11:00 UTC originate mainly from the same region at 02:00 UTC. Some are lifted relatively gently along the bent-back front in the lower layers while others are accelerated upwards within convective cells located in the middle layers. The latter create mesoscale horizontal PV dipoles whose pole reaches strongly negative values below the jet stream.~~

The same fields are shown for NODIA, also at 02:00 UTC and in the same ~~region~~ area (Fig. 10). The bent-back front is less pronounced and the corresponding updrafts are absent in NODIA (Fig. 10a). Only about ten coherent updrafts are located at upper levels. Moreover, no anticyclonic rapid segments are present. This is consistent with the absence of convective cells in the vertical cross-section and is explained by the greater stability of the middle layers compared to REF, in particular at the ~~western~~ southern edge of the cloudy area (Fig. 10b). Negative PV structures are also rare in NODIA (Fig. 10c). ~~Some~~ A few are present at upper levels, along the eastern edge of the jet stream, and are inherited from the initial conditions. The vertical cross-section illustrates the absence of horizontal PV dipoles in the mid-level troposphere (Fig. 10d). Negative PV values close to the jet stream core (around z=9 km at $\approx$56.50° N) and positive PV values in the low-level jet are both weaker compared to REF. The impact on the dynamics is contrasted at this time, as the jet stream core is not yet impacted while the low-level jet has less intense horizontal winds.

To summarize, the comparison between REF and NODIA shows the influence of cloud diabatic processes, which are at the origin of mid-level convective cells within the cloud region. These cells diabatically create horizontal PV dipoles at mid

levels with a pole reaching strongly negative values lower than $-2\,\mathrm{PVU}$. Negative PV structures then persist with time and participate in the westward extension of the ridge and the associated tightening of tropopause PV gradients, which result in the strengthening of the upper-level jet.

6 Conclusions

This paper focuses on the WCB outflow associated with the Stalactite cyclone located close to the Icelandic coast on 2 October 2016. To this end, fine-scale observations of upper-level dynamics in the WCB outflow region were performed using the RASTA radar during a flight of the Falcon 20 aircraft operated during the NAWDEX field campaign. In addition, in-situ measurements of cloud structure and dynamics were provided by four dropsondes launched from the Falcon 20. The observations are combined with results from two Meso-NH convection-permitting simulations of the cyclone during its mature phase. The first is defined as the reference simulation (REF), while in the second simulation (NODIA) heat exchanges from cloud processes are set to zero in the microphysical scheme. The main cloud structures observed by the MSG satellite are well simulated on a kilometer scale in REF, whereas the cloud tops are generally $1\,\mathrm{km}$ too low in NODIA. Moreover an abrupt eastward shift of the cyclone's trajectory, according to the ECMWF analysis, is well captured by REF but is not reproduced by NODIA.

RASTA observations show structures with low and high reflectivity values in the upper and lower troposphere, respectively. They thus highlight the presence of cirrus-type clouds in the WCB outflow region as well as convective activity within the WCB and above the Greenland Plateau. These observations combined with dropsonde measurements also reveal the existence of a dry air mass between the warm front and the Greenland Plateau. The reflectivity structures simulated in REF are in agreement with the observations, while the cloud tops are lower and the dry air mass is absent in NODIA (cutting off the diabatic cooling reduces evaporation of frozen hydrometeors under the warm front). Two regions of low dynamical tropopause are found in the simulations, a PV tongue that cuts the northwestern edge of the ridge in two parts and a tropopause fold at ~~its outer boundary~~the edge of the outer part, while local structures of negative PV are found in the inner part. In NODIA, the dynamical tropopause is lower than in REF, the tropopause fold and the PV tongue are shifted eastward, and negative PV structures are rarer.

RASTA also measures an increase in horizontal wind speed with altitude, with values locally exceeding $40\,\mathrm{m\,s^{-1}}$ associated with the jet stream around z=8 km. A low-level jet is observed along the Greenland coast with horizontal wind speed about $25\,\mathrm{m\,s^{-1}}$ below z=2 km. REF completes the measurements by highlighting the presence of two jet stream cores located near the tropopause fold and near the PV tongue. NODIA also simulates two jet stream cores but with lower intensity and shifted towards the east. Similarly, the low-level jet is well reproduced in REF but is weaker in NODIA. Dropsonde observations confirm the existence of the western jet stream core and the tropopause fold found in the simulations. They also agree with the low-level jet and dry air mass measured by RASTA.

Air parcels undergoing an ascent of at least 150 hPa in $12\,\mathrm{h}$ are identified in REF and NODIA with online Lagrangian trajectories. In REF, three main regions of ascents appear at the time of the observations. They are associated with the WCB outflow region, the cloud head and the Greenland Plateau. In contrast, only ascents located in the cloud head and above the Greenland Plateau are simulated in NODIA. They thus have a dynamical origin, due to a combination of orographic forcing and

frontal dynamics, while ascents in the WCB outflow ~~clearly arise from~~ do not occur in the absence of cloud diabatic processes. ~~The focus is on the latter, which are found in REF along the flight leg and feed the eastern jet stream core.~~

The ascents that end in the WCB outflow region are further separated between anticyclonic and cyclonic curvatures, which are approximately equally represented. Most of them start in the same region near the cyclone's bent-back front, the anticyclonic ascents being higher than the cyclonic ascents. The anticyclonic ascents end in the northwestern edge of the ridge at high altitudes and are reminiscent of the anticyclonic branch of the WCB (Martínez-Alvarado et al., 2014). The cyclonic ascents stay in the lower levels during the $12\,\mathrm{h}$ window and end further south. The rapid segments – defined as the portion of the ascents that rise by at least $100\,\mathrm{hPa}$ in $2\,\mathrm{h}$ – occur mainly in the middle troposphere along the anticyclonic ascents in the first hours of simulation and in the lower troposphere along cyclonic ascents later on. The time evolution of PV shows an increase along cyclonic ascents and a slow decrease along anticyclonic ascents. It is consistent with the vertical dipole of PV anomalies centered around the level of maximum diabatic heating described in Wernli and Davies (1997) for slantwise ascents. However, not only low but also negative PV values are reached by rapid, especially anticyclonic segments, suggesting a convective origin as in Oertel et al. (2020).

In a comparative evolution between REF and NODIA, the northwestern edge of the ridge consistently extends further west by about $100\,\mathrm{km}$ and the corresponding jet stream core is more intense and meandering. This confirms that cloud diabatic processes may reinforce the ridge and the jet stream in the WCB outflow region, as found in previous studies ~~(e.g., Chagnon et al., 2013; Joos and Forbes, 2016)~~(e.g., Chagnon et al., 2013; Schemm et al., 2013; Joos and Forbes, 2016; Maddison et a
Furthermore, elongated negative PV bands are simulated in this region in REF but not in NODIA. Such negative PV bands were also found by Blanchard et al. (2020) along the flank of a jet stream core for the same case study. Here, the comparison between REF and NODIA highlights that they are diabatically produced, in agreement with recent studies using mesoscale simulations and observations (Oertel et al., 2020; Harvey et al., 2020). The negative PV bands originate from the same region as anticyclonic ascents ending in the WCB outflow region, which leads to further examine their potential link.

During the first hours of the REF simulation, a clustering analysis identifies the updraft objects above the bent-back front, whose location matches the anticyclonic rapid segments at that time. Negative PV structures are located in the same region at mid and upper levels. While the identified updrafts in the lower layers are due to frontal dynamics and characterized by a relatively low vertical velocity of about $0.3\,\mathrm{m\,s^{-1}}$, in the middle levels they take the form of convective cells and reach about $1\,\mathrm{m\,s^{-1}}$. These cells are located at the western edge of the cloudy area, below the jet stream core and above the low-level jet, in a region of conditional instability. This description matches ~~with~~ the organized mid-level convection in the WCB region found by Blanchard et al. (2020). In addition, horizontal PV dipoles are found around the mid-level convective cells with the negative pole facing the jet stream, which confirms the theory developed in Harvey et al. (2020) and the findings of Oertel et al. (2020). In contrast, updraft objects and negative PV structures are absent from NODIA, as well as mid-level convective cells and horizontal PV dipoles.

Overall, the results highlight that negative PV structures in WCB ascent regions are diabatically created by mid-level convection. These structures are then ~~advected by the upper-level~~ transported by the anticyclonic flow into the northwestern edge of the ridge, where they persist for about $10\,\mathrm{h}$ before dispersing. During this time, they participate in extending the ridge west-

ward, strengthening PV gradients at the tropopause level and intensifying the jet stream. The results thus suggest that mid-level convection contributes to ridge building and questions its role in large-scale dynamics. As parameterization schemes often struggle to represent updrafts that do not start in the boundary layer (e.g., McTaggart-Cowan et al., 2020), the representation of mid-level convection may be a source of uncertainty for the prediction of the downstream atmospheric circulation in global models.

Code and data availability. The Meso-NH code is available on http://mesonh.aero.obs-mip.fr/ (last access: 1 December 2020). Rasta data are available from JD upon request.

Author contributions. NB performed the simulations and the analyses under the supervision of FP and JPC, JD provided the observations, and all authors prepared the manuscript.

Competing interests. The authors declare that they have no conflict of interest.

Acknowledgements. Computer resources were allocated by GENCI through ~~Project~~ project 90569. ~~The research leading to these results has received funding from the ANR-17-CE01-0010 DIP-NAWDEX project. The SAFIRE Falcon contribution to NAWDEX received direct funding from L'Institut Pierre-Simon Laplace (IPSL), Météo-France, Institut National des Sciences de l'Univers (INSU) via the LEFE program, EUFAR Norwegian Mesoscale Ensemble and Atmospheric River Experiment (NEAREX), and ESA (EPATAN, Contract 4000119015/16/NL/CT/~~
We thank the anonymous reviewers for their comments, which helped to improve the overall quality of the paper.

Financial support. The research leading to these results has received funding from the ANR-17-CE01-0010 DIP-NAWDEX project. The SAFIRE Falcon contribution to NAWDEX received direct funding from L'Institut Pierre-Simon Laplace (IPSL), Météo-France, Institut National des Sciences de l'Univers (INSU), via the LEFE program, EUFAR Norwegian Mesoscale Ensemble and Atmospheric River Experiment (NEAREX), and ESA (EPATAN, contract 4000119015/16/NL/CT/gp).

References

Blanchard, N., Pantillon, F., Chaboureau, J.-P., and Delanoë, J.: Organization of convective ascents in a warm conveyor belt, Weather Clim. Dynam., 1, 617–634, https://doi.org/10.5194/wcd-2020-25, 2020.

Browning, K. A.: Mesoscale Aspects of Extratropical Cyclones: An Observational Perspective, in: The Life Cycles of Extratropical Cyclones, edited by Shapiro M.A., Grønås S., American Meteorological Society, pp. 265–283, https://doi.org/10.1007/978-1-935704-09-6_18, 1999.

Chagnon, J. M., Gray, S. L., and Methven, J.: Diabatic processes modifying potential vorticity in a North Atlantic cyclone, Q. J. Roy. Meteorol. Soc., 139, 1270–1282, https://doi.org/10.1002/qj.2037, 2013.

Colella, P. and Woodward, P. R.: The Piecewise Parabolic Method (PPM) for gas-dynamical simulations, J. Comput. Phys., 54, 174–201, https://doi.org/10.1016/0021-9991(84)90143-8, 1984.

Dauhut, T., Chaboureau, J.-P., Escobar, J., and Mascart, P.: Giga-LES of Hector the Convector and its two tallest updrafts up to the stratosphere, J. Atmos. Sci., 73, 5041–5060, https://doi.org/10.1175/JAS-D-16-0083.1, 2016.

Delanoë, J., Protat, A., Jourdan, O., Pelon, J., Papazzoni, M., Dupuy, R., Gayet, J.-F., and Jouan, C.: Comparison of airborne in situ, airborne radar-lidar, and spaceborne radar-lidar retrievals of polar ice cloud properties sampled during the POLARCAT campaign, J. Atmos. Ocean Technol., 30, 57–73, https://doi.org/10.1175/JTECH-D-11-00200.1, 2013.

Gheusi, F. and Stein, J.: Lagrangian description of airflows using Eulerian passive tracers, Q. J. Roy. Meteorol. Soc., 128, 337–360, https://doi.org/10.1256/00359000260498914, 2002.

Grams, C. M., Wernli, H., Böttcher, M., Čampa, J., Corsmeier, U., Jones, S. C., Keller, J. H., Lenz, C.-J., and Wiegand, L.: The key role of diabatic processes in modifying the upper-tropospheric wave guide: a North Atlantic case-study, Q. J. Roy. Meteorol. Soc., 137, 2174–2193, https://doi.org/10.1002/qj.891, 2011.

Gray, S. L., Dunning, C. M., Methven, J., Masato, G., and Chagnon, J. M.: Systematic model forecast error in Rossby wave structure, Geophys. Res. Lett., 41, 2979–2987, https://doi.org/10.1002/2014GL059282, 2014.

Harrold, T. W.: Mechanisms influencing the distribution of precipitation within baroclinic disturbances, Q. J. Roy. Meteorol. Soc., 99, 232–251, https://doi.org/10.1002/qj.49709942003, 1973.

Harvey, B., Methven, J., Sanchez, C., and Schäfler, A.: Diabatic generation of negative potential vorticity and its impact on the North Atlantic jet stream, Q. J. Roy. Meteorol. Soc., 146, 1477–1497, https://doi.org/10.1002/qj.3747, 2020.

Hoskins, B. J. and Ambrizzi, T.: Rossby Wave Propagation on a Realistic Longitudinally Varying Flow, J. Atmos. Sci., 50, 1661–1671, https://doi.org/10.1175/1520-0469(1993)050<1661:RWPOAR>2.0.CO;2, 1993.

Hoskins, B. J., McIntyre, M. E., and Robertson, A. W.: On the use and significance of isentropic potential vorticity maps, Q. J. Roy. Meteorol. Soc., 111, 877–946, https://doi.org/10.1002/qj.49711147002, 1985.

Joos, H. and Forbes, R. M.: Impact of different IFS microphysics on a warm conveyor belt and the downstream flow evolution, Q. J. Roy. Meteorol. Soc., 142, 2727–2739, https://doi.org/10.1002/qj.2863, 2016.

Lac, C., Chaboureau, J.-P., Masson, V., Pinty, J.-P., Tulet, P., Escobar, J., Leriche, M., Barthe, C., Aouizerats, B., Augros, C., Aumond, P., Auguste, F., Bechtold, P., Berthet, S., Bieilli, S., Bosseur, F., Caumont, O., Cohard, J.-M., Colin, J., Couvreux, F., Cuxart, J., Delautier, G., Dauhut, T., Ducrocq, V., Filippi, J.-B., Gazen, D., Geoffroy, O., Gheusi, F., Honnert, R., Lafore, J.-P., Lebeaupin Brossier, C., Libois, Q., Lunet, T., Mari, C., Maric, T., Mascart, P., Mogé, M., Molinié, G., Nuissier, O., Pantillon, F., Peyrillé, P., Pergaud, J., Perraud, E., Pianezze, J., Redelsperger, J.-L., Ricard, D., Richard, E., Riette, S., Rodier, Q., Schoetter, R., Seyfried, L., Stein, J., Suhre, K., Thouron, O., Turner,

S., Verrelle, A., Vié, B., Visentin, F., Vionnet, V., and Wautelet, P.: Overview of the Meso-NH model version 5.4 and its applications, Geosci. Model Dev., 11, 1929–1969, https://doi.org/10.5194/gmd-11-1929-2018, 2018.

Maddison, J. W., Gray, S. L., Martínez-Alvarado, O., and Williams, K. D.: Upstream Cyclone Influence on the Predictability of Block Onsets over the Euro-Atlantic Region, Mon. Weather Rev., 147, 1277–1296, https://doi.org/10.1175/MWR-D-18-0226.1, 2019.

Maddison, J. W., Gray, S. L., Martínez-Alvarado, O., and Williams, K. D.: Impact of model upgrades on diabatic processes in extratropical cyclones and downstream forecast evolution, Q. J. Roy. Meteorol. Soc., 146, 1322–1350, https://doi.org/10.1002/qj.3739, 2020.

Martínez-Alvarado, O., Maddison, J. W., Gray, S. L., and Williams, K. D.: Atmospheric blocking and upper-level Rossby-wave forecast skill dependence on model configuration, Q. J. Roy. Meteorol. Soc., 144, 2165–2181, https://doi.org/10.1002/qj.3326, 2018.

Martínez-Alvarado, O., Joos, H., Chagnon, J., Boettcher, M., Gray, S. L., Plant, R. S., Methven, J., and Wernli, H.: The dichotomous structure of the warm conveyor belt, Q. J. Roy. Meteorol. Soc., 140, 1809–1824, https://doi.org/10.1002/qj.2276, 2014.

McTaggart-Cowan, R., Vaillancourt, P. A., Separovic, L., Corvec, S., and Zadra, A.: A Convection Parameterization for Low-CAPE Environments, Mon. Weather Rev., p. in press, https://doi.org/10.1175/MWR-D-20-0020.1, 2020.

Oertel, A., Boettcher, M., Joos, H., Sprenger, M., and Wernli, H.: Potential vorticity structure of embedded convection in a warm conveyor belt and its relevance for large-scale dynamics, Weather Clim. Dynam., 1, 127–153, https://doi.org/10.5194/wcd-1-127-2020, 2020.

Schemm, S., Wernli, H., and Papritz, L.: Warm Conveyor Belts in Idealized Moist Baroclinic Wave Simulations, J. Atmos. Sci., 70, 627–652, https://doi.org/10.1175/JAS-D-12-0147.1, 2013.

Schäfler, A., Craig, G., Wernli, H., Arbogast, P., Doyle, J. D., McTaggart-Cowan, R., Methven, J., Rivière, G., Ament, F., Boettcher, M., Bramberger, M., Cazenave, Q., Cotton, R., Crewell, S., Delanoë, J., Dörnbrack, A., Ehrlich, A., Ewald, F., Fix, A., Grams, C. M., Gray, S. L., Grob, H., Groß, S., Hagen, M., Harvey, B., Hirsch, L., Jacob, M., Kölling, T., Konow, H., Lemmerz, C., Lux, O., Magnusson, L., Mayer, B., Mech, M., Moore, R., Pelon, J., Quinting, J., Rahm, S., Rapp, M., Rautenhaus, M., Reitebuch, O., Reynolds, C. A., Sodemann, H., Spengler, T., Vaughan, G., Wendisch, M., Wirth, M., Witschas, B., Wolf, K., and Zinner, T.: The North Atlantic Waveguide and Downstream Impact Experiment, Bull. Amer. Meteo. Soc., 99, 1607–1637, https://doi.org/10.1175/BAMS-D-17-0003.1, 2018.

Schäfler, A., Harvey, B., Methven, J., Doyle, J. D., Rahm, S., Reitebuch, O., Weiler, F., and Witschas, B.: Observation of Jet Stream Winds during NAWDEX and Characterization of Systematic Meteorological Analysis Errors, Mon. Weather Rev., 148, 2889–2907, https://doi.org/10.1175/MWR-D-19-0229.1, 2020.

Steinfeld, D., Boettcher, M., Forbes, R., and Pfahl, S.: The sensitivity of atmospheric blocking to upstream latent heating – numerical experiments, Weather and Climate Dynamics, 1, 405–426, https://doi.org/10.5194/wcd-1-405-2020, 2020.

Söhne, N., Chaboureau, J.-P., and Guichard, F.: Verification of cloud cover forecast with satellite observation over West Africa, Mon. Weather Rev., 136, 4421–4434, https://doi.org/10.1175/2008MWR2432.1, 2008.

Wernli, H. and Davies, H. C.: A Lagrangian-based analysis of extratropical cyclones. I: The method and some applications, Q. J. Roy. Meteorol. Soc., 123, 467–489, https://doi.org/10.1002/qj.49712353811, 1997.

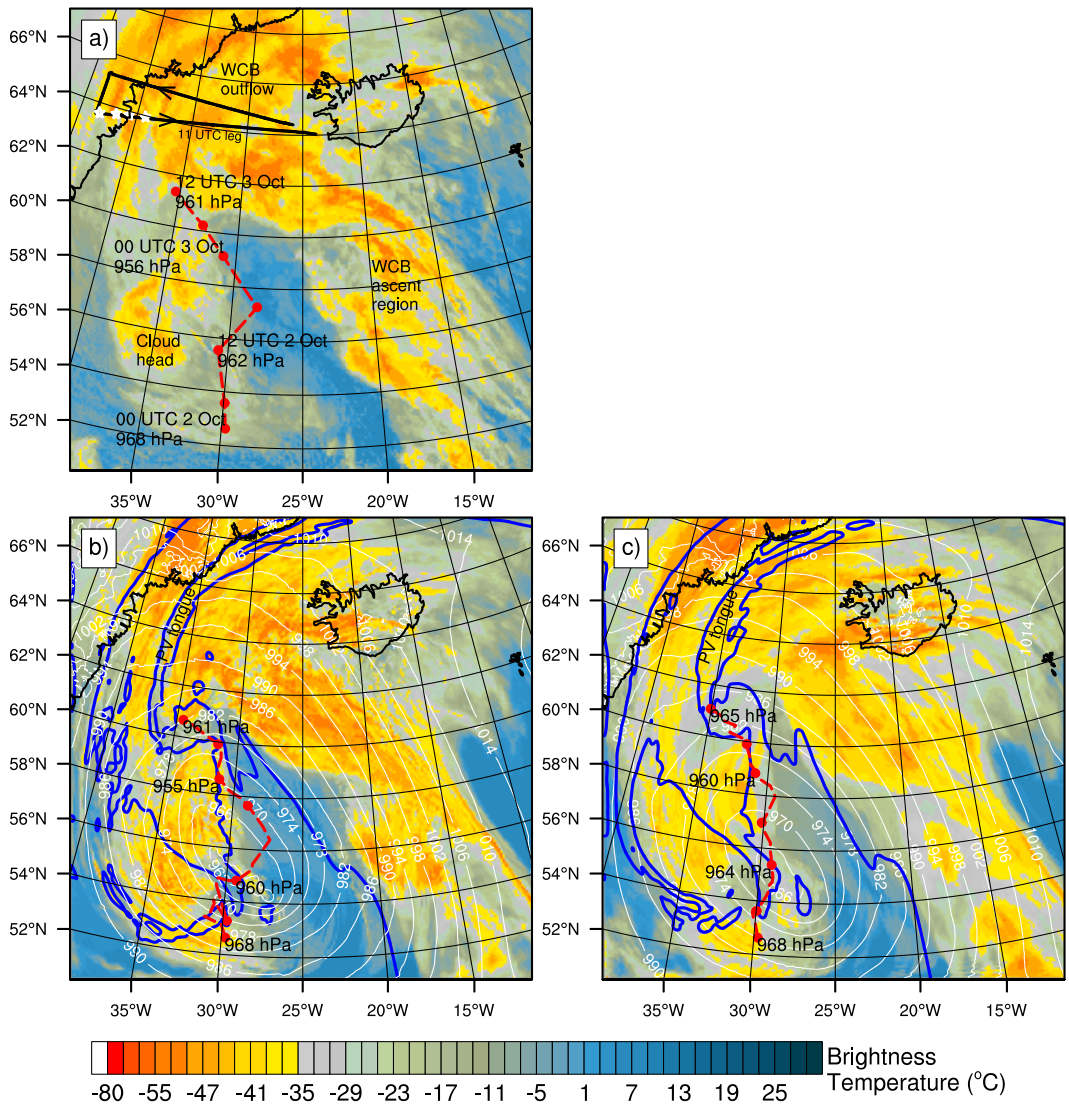

Figure 1. 10.8 μm brightness temperature (in °C) at 11:00 UTC, 2 October 2016 as (a) observed by MSG and simulated by (b) REF and (c) NODIA. In (b) and (c), MSLP is shown with white contours every 4 hPa between 964 and 1016 hPa and the smoothed 2 PVU at 320 K with blue contours. In (a), (b) and (c), the cyclone track and value of the MSLP minimum are shown (red dotted line, red mark every 3 h) for the ECMWF analysis, REF and NODIA, respectively. The MSLP minimum is tracked every 6 h within a radius of 250 km from its prior position in the ECMWF analysis and every 1 h within a radius of 160 km in the simulations. In (a), the black line shows the track of the Falcon 20 aircraft and the 11:00 UTC leg whereas the white stars show the location of the dropsondes shown in Fig. 4.~~In (b) and (c), MSLP is shown with white contours every 4 between 964 and 1016 and the smoothed 2 at 320 with blue contours.~~

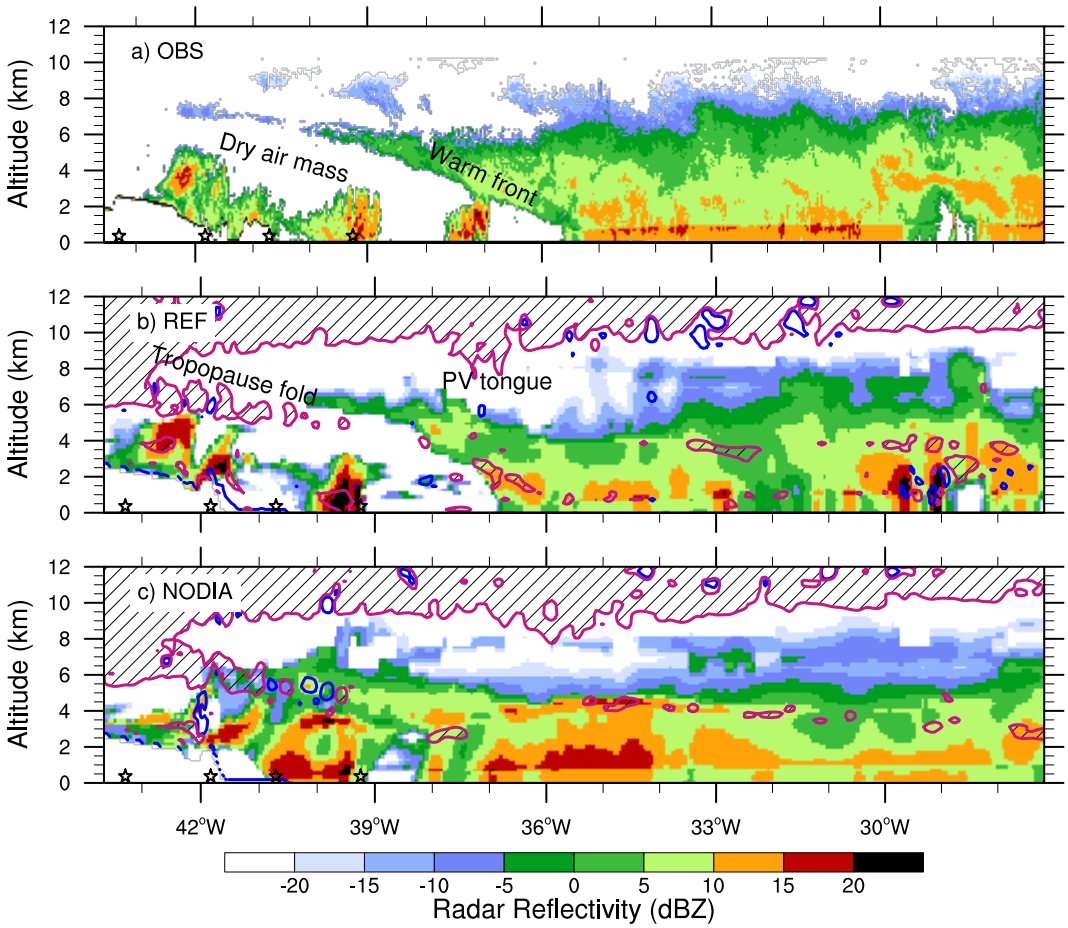

Figure 2. Reflectivity (in dBZ) (a) measured by RASTA and simulated by (b) REF and (c) NODIA along the 11:00 UTC leg (black line in Fig. 1). The black stars show the position of the dropsondes shown in Fig. 4. In (b) and (c), magenta and navy blue contours show PV values equal to 2 PVU and −1 PVU, respectively, with hatching for PV values greater than 2 PVU.

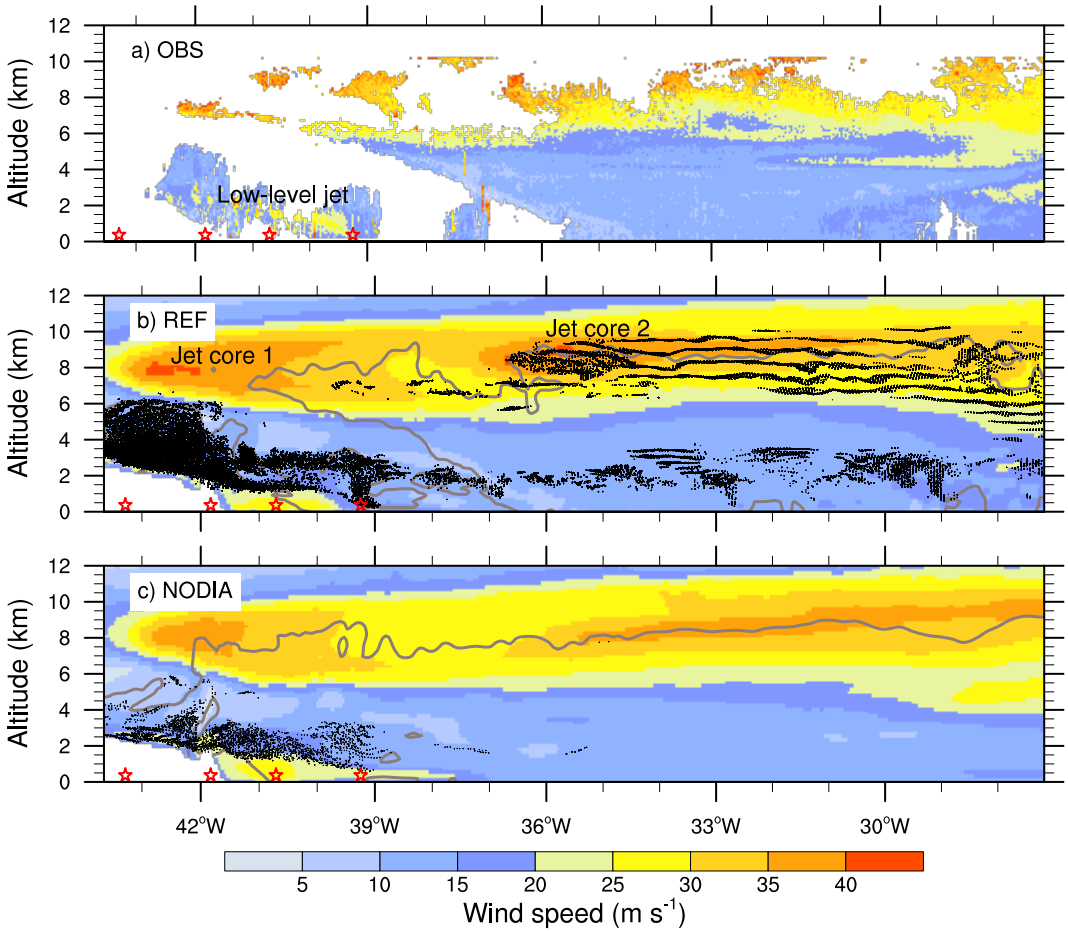

Figure 3. Horizontal wind speed (in $\mathrm{m\,s^{-1}}$) (a) measured by RASTA and simulated by (b) REF and (c) NODIA along the 11:00 UTC leg (black line in Fig. 1). The red stars indicate the position of the dropsondes shown in Fig. 4. In (b) and (c), the black dots indicate the position of the selected ascents (see text for details) and the grey lines show the condensed water content equal to $0.02\,\mathrm{g\,kg^{-1}}$.

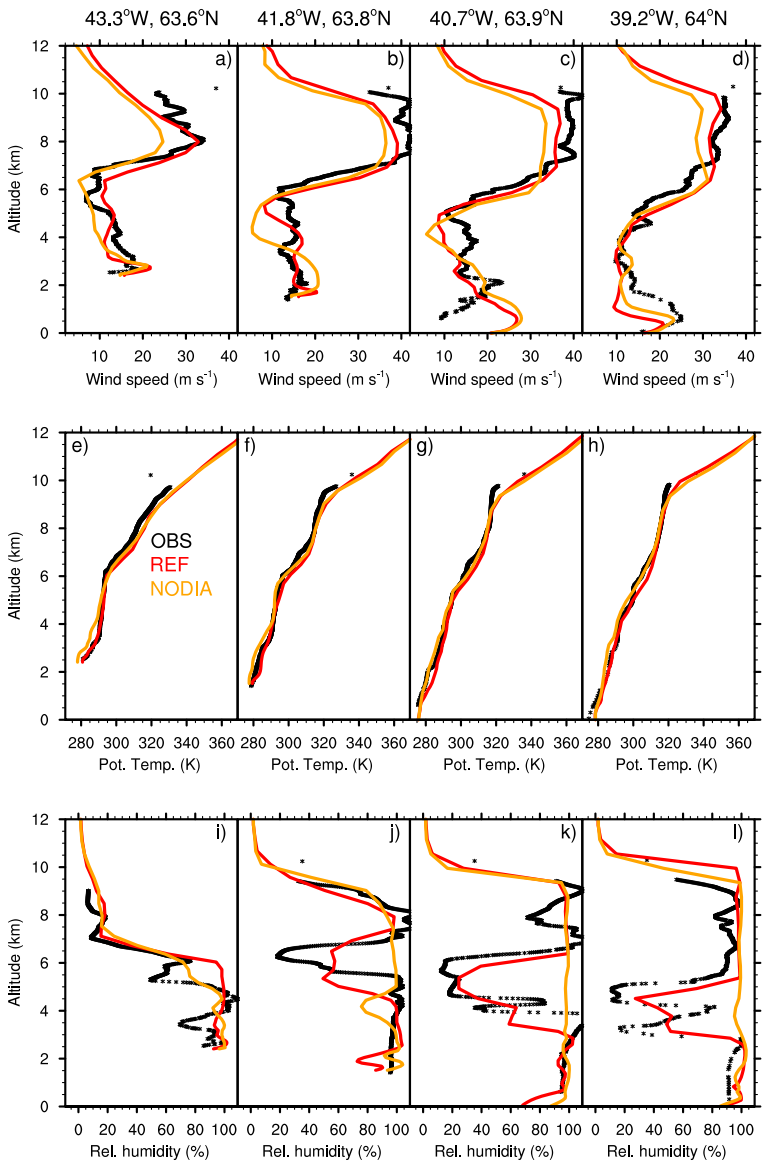

Figure 4. Profiles of (a–d) wind speed, (e–h) potential temperature and (i–l) relative humidity at (a, e, f) 43.3° W, 63.6° N, (b, f, j) 41.8°W, 63.8° N, (c, g, k) 40.7° W, 63.9° N and (d, h, l) 39.2° W, 64° N launched at 10:26, 10:32, 10:36 and 10:41 UTC, respectively. Their location is shown as white stars in Fig. 1a. The measurements by dropsondes are shown with black lines and the REF and NODIA simulations with red and orange lines, respectively.

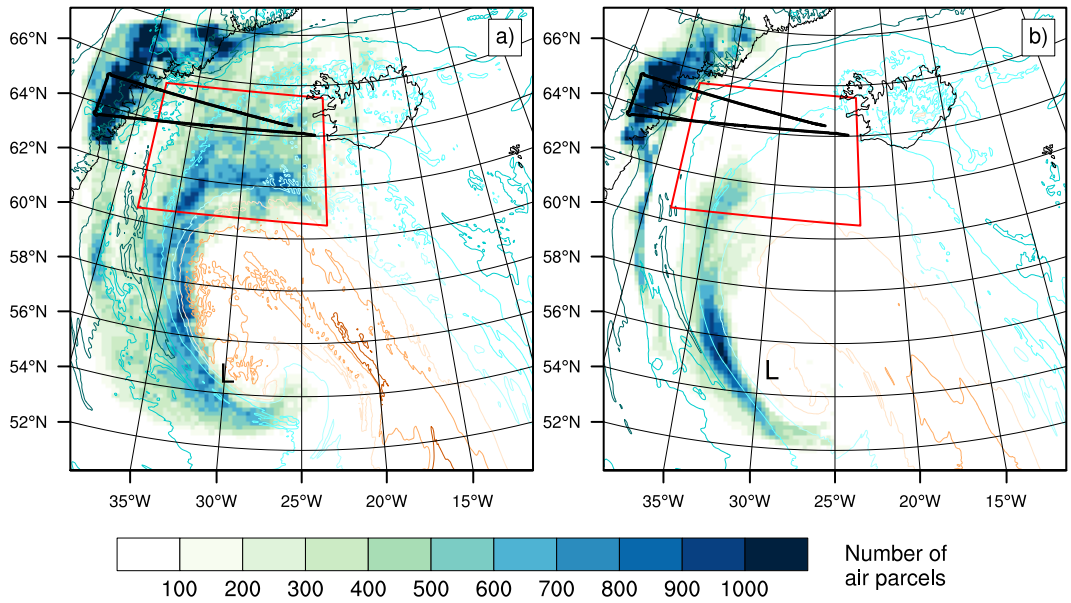

Figure 5. ~~Spatial frequency~~ Number of air parcels belonging to the ascents fulfilling the ascent criterion (shading) and θ_e at 1 km altitude (colored lines every 4 K between 288 and 312 K) at 11:00 UTC simulated by (~~a)~~ **a)** REF and (~~b)~~ **b)** NODIA. The black line shows the track of the Falcon 20 aircraft, L the low-pressure center and the red box the region where the ascents are selected at 11:00 UTC.

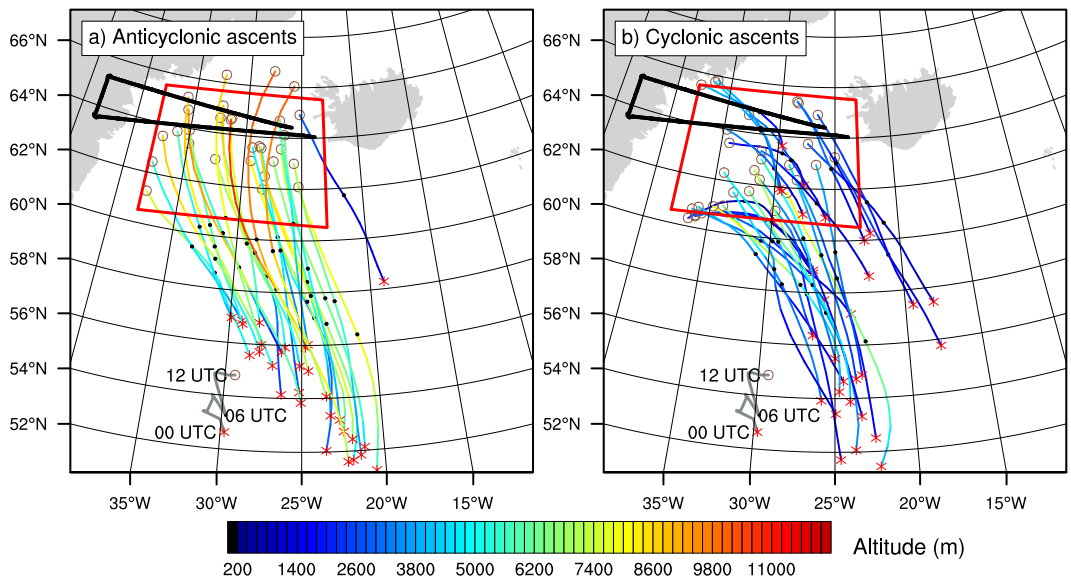

Figure 6. Selected trajectories colored by altitude between 00:00 and 12:00 UTC for ~~(a)~~ **(a)** anticyclonic ascents and ~~(b)~~ **(b)** cyclonic ascents simulated by REF. Only ~~40~~ 30 trajectories (out of 220 000 anticyclonic ascents and out of 250 000 cyclonic ascents) are plotted for each category of ascents. A red cross, a black dot and a brown circle show the location of each trajectory at 00:00, 06:00 and 12:00 UTC, respectively. The black line shows the track of the Falcon 20 aircraft, the grey line the position of the MSLP minimum and the red box the region where the ascents are selected at 11:00 UTC.

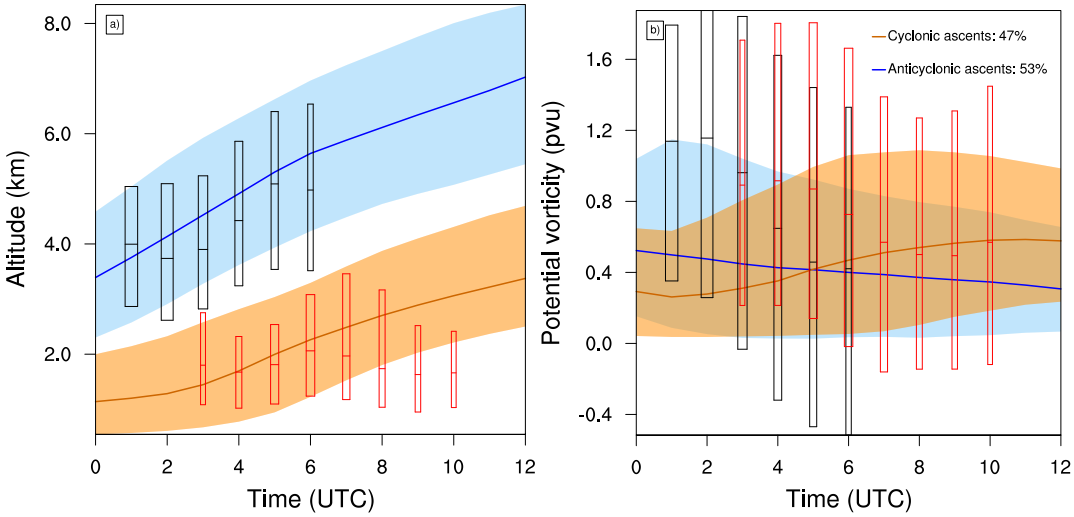

Figure 7. Time evolution of (a) altitude (in km) and (b) PV (in PVU) between 00:00 and 12:00 UTC along the selected trajectories in REF. The median (colored bold line) and the 25th-75th percentiles (shaded color) are shown for cyclonic (orange) and anticyclonic (blue) ascents. The median and the 25th-75th percentiles are shown with boxplots for the 2 h rapid cyclonic (red) and anticyclonic (black) segments. Boxplots are displayed only where the number of rapid segments lies above their time average and their width is scaled with this number.

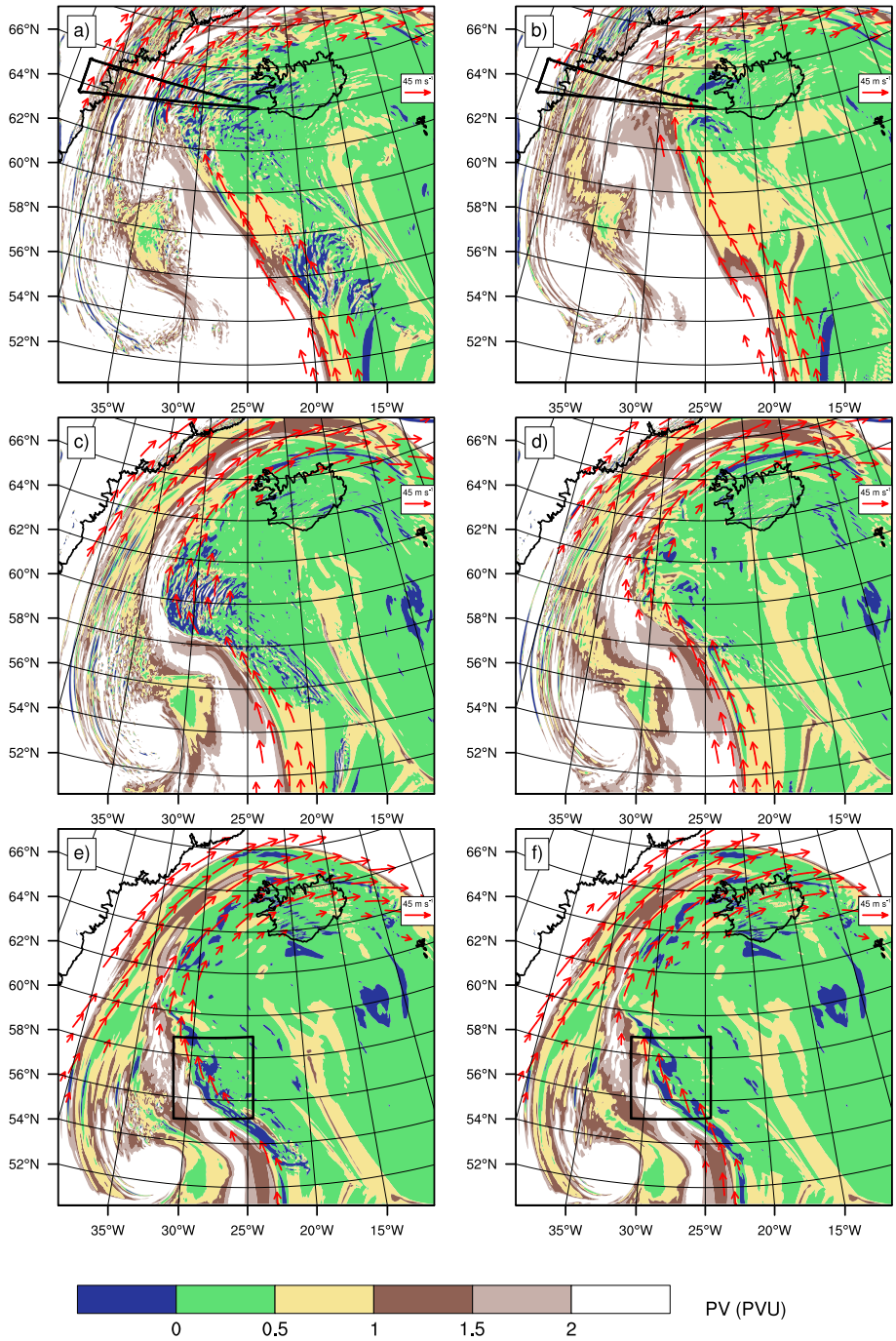

Figure 8. PV (shading) and wind above 45 $\mathrm{m\,s^{-1}}$ (red arrows) on the 320 K level at (a, b) 11:00 UTC, (c, d) 06:00 UTC and (e, f) 02:00 UTC simulated by (a, c, e) REF and (b, d, f) NODIA. The black line in (a, b) shows the track of the Falcon 20 aircraft and the box in (e, f) indicates the zoom in Figs. 9 and 10.

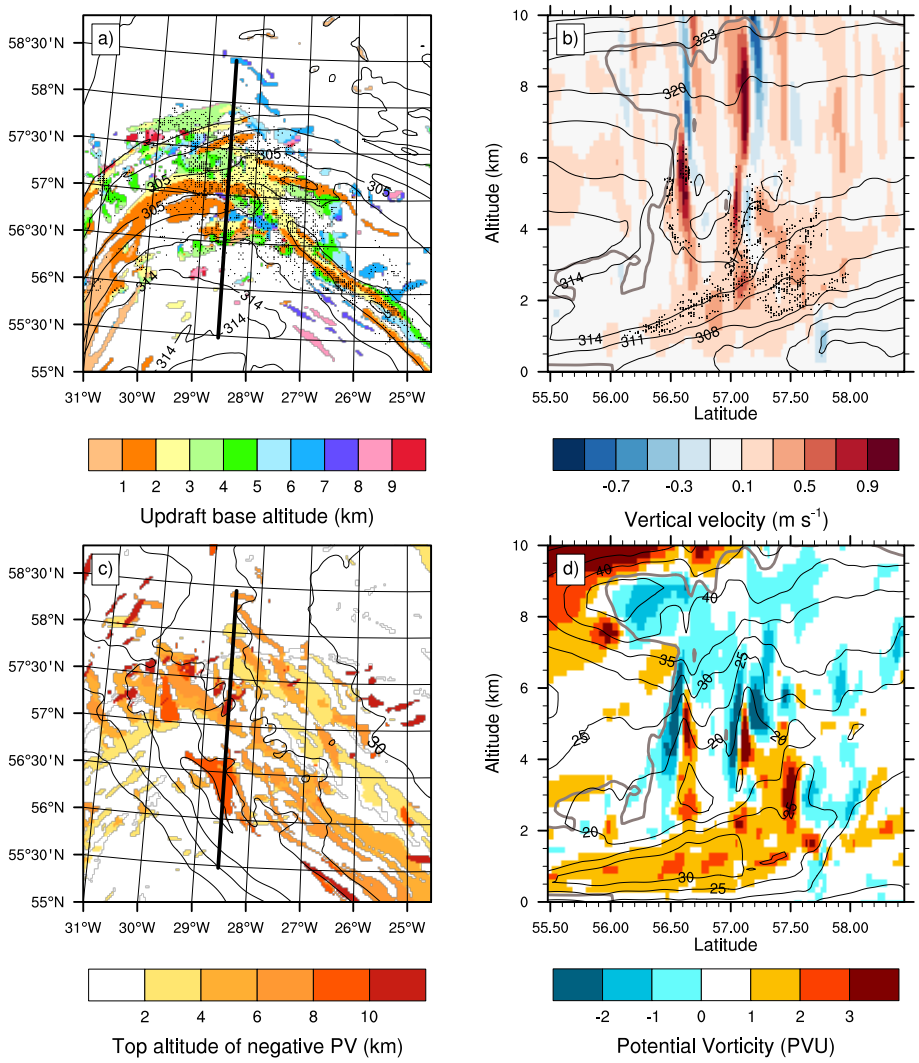

Figure 9. ~~Updrafts and potential vorticity~~ Results at 02:00 UTC ~~in~~ for the REF simulation: (a) base altitude of updrafts (shading, in km) and θ_e at 1 km height (black contours every 3 K); (b) vertical velocity (shading, in $\mathrm{m\,s^{-1}}$), θ_e (black contours every 3 K) and cloud variables (thick grey contour above 0.1 $\mathrm{g\,kg^{-1}}$) along the vertical cross-section illustrated in (a); (c) top altitude of negative PV structures (shading, in km) and horizontal wind speed on the 320 K level (contours every 5 K above 30 $\mathrm{m\,s^{-1}}$); (d) PV (shading, in PVU), horizontal wind speed (black contours every 5 K) and cloud variables (thick grey contour above 0.1 $\mathrm{g\,kg^{-1}}$) along the vertical cross-section illustrated in (b). Dots in (a, b) indicate the location of rapid anticyclonic segments, reduced to one every 10 in (a).

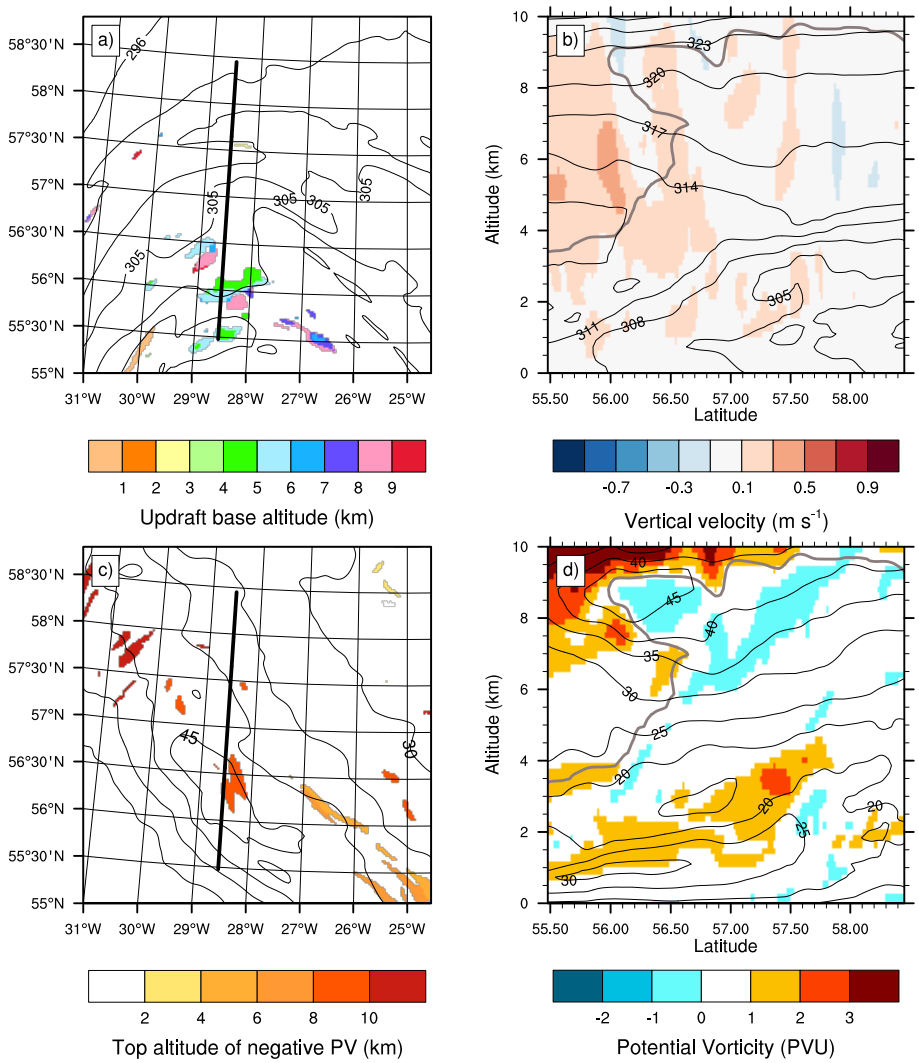

Figure 10. As in Fig. 9 but for the NODIA simulation.